Volume 14
Number 24
23 April 2026
Pages 14653–15486

Journal of Materials Chemistry A

Materials for energy and sustainability

rsc.li/materials-a

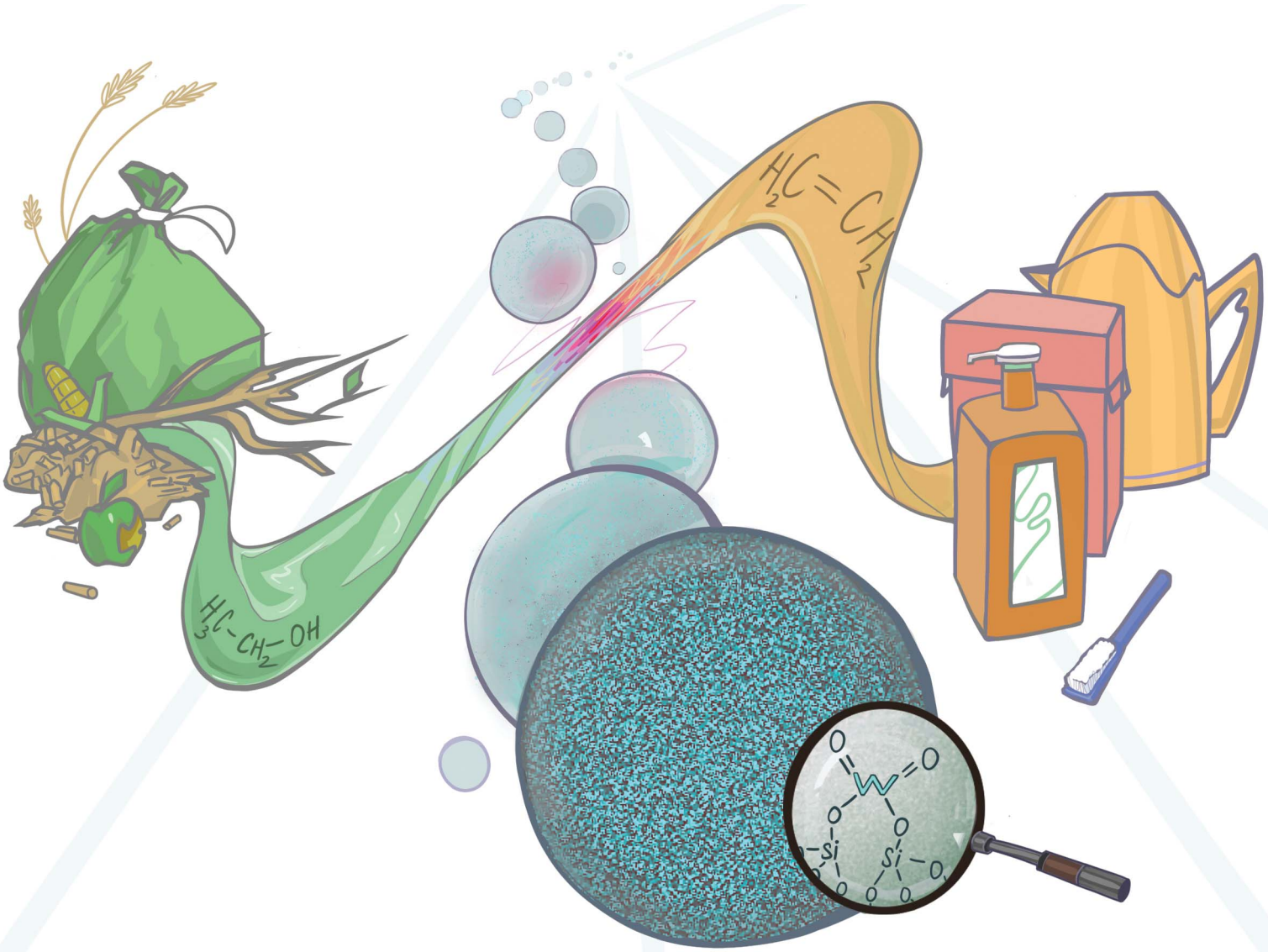

ISSN 2050-7488

ROYAL SOCIETY OF CHEMISTRY

PAPER

David Skoda, Ales Styskalik, Damien P. Debecker *et al.*
Microwave-assisted one-pot sol–gel synthesis of tungsten silicate microspheres with dispersed WO_x and their activity in ethanol dehydration

Journal of Materials Chemistry A

ROYAL SOCIETY OF CHEMISTRY

PAPER

View Article Online
View Journal | View Issue

Cite this: J. Mater. Chem. A, 2026, 14, 14866

Microwave-assisted one-pot sol–gel synthesis of tungsten silicate microspheres with dispersed WO_x and their activity in ethanol dehydration

David Skoda, *[a] Tomas Pokorny, [b] Barbora Hanulikova, [a] Ales Styskalik, *[b] Zuzana Hlavenkova, [c] Lucie Simonikova, [b] Jan Varada, [b] Lucie Leonova, [b] Ivo Kuritka, [a] Claude Poleunis[d] and Damien P. Debecker *[d]

This study introduces a novel microspherical W–SiO_2 heterogeneous catalyst for alcohol dehydration, prepared *via* an innovative microwave-assisted condensation synthesis method. The process involves the microwave-assisted preparation of a hybrid tungsten naphthalene dicarboxylate-based precursor solution, which is subsequently condensed with (3-aminopropyl)triethoxysilane in a single step—eliminating the need for separate silica support preparation, as required in conventional impregnation methods. After calcination at 550 °C, the resulting amorphous and porous microspheres contain highly dispersed tungsten species (with loadings of 2, 6, and 12 wt%), with no crystalline WO_3 phase detected, even at the highest loading. Compared to a 12 wt% WO_3/SiO_2 catalyst prepared *via* conventional impregnation, the W–SiO_2 microspheres exhibit higher catalytic activity and ethylene selectivity in ethanol dehydration at 420 °C. Notably, the 2W–SiO_2 catalyst achieved the highest initial ethylene productivity per mole of tungsten (520 mmol $mmol_W^{-1}$ h^{-1}), maintaining 230 mmol $mmol_W^{-1}$ h^{-1} after 1000 minutes on stream, indicating high long-term stability. In terms of mass-specific performance, the 12W–SiO_2 catalyst reached 133 mmol g^{-1} h^{-1}, outperforming other comparable previously reported tungsten–silica catalysts.

Received 1st October 2025
Accepted 12th March 2026

DOI: 10.1039/d5ta08046k

rsc.li/materials-a

1 Introduction

Ethylene is one of the world's most important chemical commodities, serving as a key building block for the synthesis of major derivatives such as polyethylene, vinyl chloride, ethylene oxide, ethylbenzene, and poly(ethylene terephthalate). Currently, ethylene production relies predominantly on the steam cracking of petroleum-based feedstocks.[1] However, the growing global demand for alkene compounds is driving increased consumption of fossil fuels and oil resources. This situation underscores the urgent need for sustainable alternatives to conventional alkene production. One promising route is the dehydration of (biomass-derived) alcohols to produce alkenes. Ethanol, in particular, stands out as a highly sustainable and readily available feedstock for the ethanol-to-ethylene (ETE) process.[1,2] Traditionally, alcohol dehydration requires elevated temperatures and strong acids, making the development of efficient heterogeneous catalysts essential for enabling milder reaction conditions and reducing energy consumption in the ETE process. Utilizing biomass-derived ethanol for ethylene production can significantly lower greenhouse gas emissions and reduce dependence on finite fossil resources,[3] contributing to the achievement of Sustainable Development Goals (SDGs), namely SDG7 (Affordable and Clean Energy), SDG 9 (Industry, Innovation and Infrastructure), SDG 12 (Responsible Consumption and Production), and SDG 13 (Climate Action).[4]

Tungsten-containing catalysts have demonstrated notable activity and selectivity in alcohol dehydration to alkenes,[1,5–8] olefin metathesis,[9,10] and dehydration of glucose[11] and glycerol.[12] The catalytic performance of these systems depends on several factors, including the nature of the tungsten species, the choice of support material, and reaction conditions. In particular, tungsten oxide (WO_x) supported on silica exhibits unique properties that promote high ethanol dehydration activity.[6] The interaction between tungsten and silica stabilizes the active species and boosts overall catalytic activity. For example, WO_3 supported on mesoporous structures such as mesocellular foam silica (MCF-Si) and SBA-15 has shown excellent performance in the ETE process. Among these, WO_3/MCF-Si catalysts have achieved ethylene yields of up to 96.6% under vapor-phase conditions at 400 °C, even with dilute ethanol feeds (70% v/v),

[a]Centre of Polymer Systems, Tomas Bata University in Zlín, tr. Tomase Bati 5678, Zlín, CZ-76001, Czech Republic. E-mail: dskoda@utb.cz

[b]Department of Chemistry, Faculty of Science, Masaryk University, Kotlarska 2, Brno, CZ-61137, Czech Republic. E-mail: styskalik@chemi.muni.cz

[c]Central European Institute of Technology, Masaryk University, Kamenice 5, Brno, CZ 62500, Czech Republic

[d]Institute of Condensed Matter and Nanosciences (IMCN), Université catholique de Louvain (UCLouvain), Place Louis Pasteur 1, 1348 Louvain-La-Neuve, Belgium. E-mail: damien.debecker@uclouvain.be

and maintain stability over extended operation without regeneration.[6,13]

A common synthesis method for WO_x/SiO_2 heterogeneous catalysts is impregnation, where a precursor solution is deposited onto a silica support followed by calcination.[6,8,13–17] For instance, WO_3/SiO_2 catalysts are typically prepared *via* incipient wetness impregnation of ammonium tungstate onto silica, followed by calcination at around 550 °C.[17] Calcination not only ensures a well-dispersed active phase but also enhances thermal stability, which is crucial for sustained catalytic performance. Beyond classical impregnation, innovative techniques such as microwave-assisted grafting, aerosol-assisted, and non-hydrolytic preparation methods have emerged.[18–20] These methods facilitate the rapid and uniform distribution of WO_3 on silica substrates, enhancing catalyst activity and selectivity in reactions such as glycerol dehydration to acrolein or olefin metathesis.[18–20] Specifically, in the case of olefin metathesis the isolated and highly dispersed W(VI)–dioxo sites are of tremendous importance to achieve high catalytic performance.[9] Microwave-assisted methods, in particular, optimize the grafting of metal oxides onto colloidal silica, significantly enhancing functional performance compared to conventional heating. Additional advanced methods include aerosol processes combined with surfactant-templated sol–gel synthesis,[21] and template-free sol–gel methods assisted by supercritical CO_2 drying.[22]

Tungsten-based catalysts can exhibit both Brønsted and Lewis acidity,[12,23–25] with each type contributing to the catalytic activity in alcohol dehydration reactions.[26–28] The mechanism for ethanol dehydration over these catalysts generally involves ethanol adsorption, protonation, and subsequent water elimination, ultimately forming ethylene.[29,30] This process typically follows a unimolecular elimination (E1) pathway, where the initial cleavage of the C–O bond is the rate-determining step, followed by β-hydrogen elimination to generate the C=C bond.[31] The distribution and strength of Brønsted and Lewis acid sites on the catalyst surface play a crucial role in determining product selectivity, with optimal conditions favoring high ethylene yields.[29] The amount of tungsten loaded onto the silica support also significantly impacts catalytic performance; an optimal loading maximizes the number of active sites while minimizing steric hindrance.[32] Additionally, the stability and durability of tungsten-silica catalysts under specific reaction conditions are essential for their practical implementation. Catalyst deactivation, often due to coking or sintering, presents a significant challenge in maintaining catalytic performance over time.[33] It has also been reported that the hydrophobicity and hydrophilicity of heterogeneous catalysts used in reactions that generate water play an important role in catalyst stability and overall performance.[34] Recent advancements in catalyst design—such as the incorporation of mesoporous structures and hybrid materials—have been explored to enhance the stability and activity of tungsten-based catalysts.[35,36] These innovations aim to create more robust catalytic frameworks capable of withstanding the demanding conditions typical of ethanol dehydration processes. Despite these advances, the rapid and one-step synthesis of stable, reusable catalysts with a homogeneous distribution of tungsten, high activity, and selectivity at moderate temperatures remains a significant challenge.

We have recently introduced a facile preparation technique for vanadium- or molybdenum-silicate microspheres and shown their application as heterogeneous catalysts for epoxidation reactions and propylene metathesis, respectively.[37–39] We have demonstrated that the developed synthetic procedure leads to a highly homogeneous dispersion of molybdate or vanadate species in the microspheres compared to the catalysts prepared by incipient wetness impregnation. Based on these findings we developed an original preparation method for tungsten-silicate microspheres with homogeneously dispersed tungstate species.

A microwave-assisted sol–gel condensation method allows the fabrication of W–SiO_2 catalysts tailored for alcohol dehydration. The synthesis begins with the microwave-assisted preparation of a hybrid precursor solution comprising tungsten hexacarbonyl and 2,6-naphthalene dicarboxylic acid, which is subsequently condensed with (3-aminopropyl)triethoxysilane. This reaction leads to the precipitation of a hybrid tungsten silicate solid precursor. Upon calcination, the final inorganic W–SiO_2 microspheres are obtained. This streamlined one-pot approach eliminates the need for separate silica support synthesis. Moreover, the method enables the formation of highly dispersed and homogeneously distributed tungsten active sites within the silica matrix, which significantly enhances the catalytic performance of the resulting W–SiO_2 microspheres.

2 Experimental

2.1 Chemicals

Tungsten hexacarbonyl ($W(CO)_6$, M_w 351.9 g mol^{-1}, 99%), 2,6-naphthalenedicarboxylic acid (H_2NDC, M_w 216.19 g mol^{-1}, 95%), (3-aminopropyl)triethoxysilane ($H_2N(CH_2)_3Si(OC_2H_5)_3$, APTES, M_w 221.37 g mol^{-1}, 99%), ammonium metatungstate hydrate ($(NH_4)_6H_2W_{12}O_{40}\cdot xH_2O$, M_w 2956.3 g mol^{-1}, 99%), and a silica support (Normasil 60) were supplied from Merck. *N*,*N*′-Dimethylformamide (DMF, p.a., 99.5%) and absolute ethanol (UV-vis spectroscopy grade, 99.8%) were purchased from Penta Chemicals (Czech Republic).

2.1.1 Synthesis of W–SiO_2 microspheres. Tungsten hexacarbonyl ($W(CO)_6$) (the mass for each W loading is specified in SI, Table S1) was dissolved in a mixture of 50 mL of *N*,*N*′-dimethylformamide (DMF), 0.5 mL of ultra-pure water (UPW), and 0.5 mL of absolute ethanol in a Teflon container. After the dissolution of the tungsten precursor, 2,6-naphthalenedicarboxylic acid (H_2NDC) was added, and the container was closed, placed in a microwave reactor (ERTEC Magnum II; 600 W; 2.45 GHz), and securely sealed. The microwave power was set to 70% (420 W), and the reaction mixture was heated to 180 °C for 40 minutes under microwave irradiation, reaching the target temperature in approximately 10 minutes (Fig. 1S). The resulting hybrid intermediate from the microwave-assisted reaction was denoted as W–NDC. Once cooled to room temperature, the yellow transparent W–NDC precursor solution

was gradually added to a stirred solution of (3-aminopropyl) triethoxysilane (APTES, 1.18 g, 5.33 mmol) in 50 mL of DMF. After the whole volume of W–NDC precursor solution was mixed with APTES, a yellow transparent solution was obtained, and in *ca.* 10 minutes, the mixture became cloudy, followed by the formation of a white precipitate. The mixture was continuously stirred at room temperature for 4 hours. The precipitate formed during the condensation of the W–NDC precursor and APTES (labeled as W–NDC–Si) was separated by centrifugation (6000 rpm, 5 minutes), and dried in an oven at 80 °C overnight. The amount of each separated hybrid W–NDC–Si solid precursor was *ca.* 0.60–0.68 g.

The W–NDC–Si solid precursors were calcined in a muffle furnace at 550 °C (heating ramp rate of 5 °C min^{-1}) for 3 hours under an air atmosphere to generate inorganic W–SiO_2-based samples, which were utilized as catalysts for alcohol dehydration. Three samples denoted as 12W–SiO_2, 6W–SiO_2, and 2W–SiO_2 were prepared in total with the numbers at the beginning of the sample label referring to different W loadings.

2.1.2 12W–SiO_2–WI. For comparison purposes, the 12W–SiO_2–WI sample was prepared *via* a direct wet impregnation (WI) method. Chromatographic silica (Normasil 60) was used as the support, with 5.000 g employed for the preparation. Ammonium metatungstate hydrate (1.054 g) was dissolved in 400 mL of demineralized water and thoroughly mixed with the silica. The mixture was continuously stirred on a hot plate at 60 °C while the water was slowly evaporated. The resulting dry powder was then calcined in ambient air at 550 °C for 5 hours. The content of W in the 12W–SiO_2–WI sample according to ICP-OES is 11.6 wt%.

2.1.3 4W–SiO_2-imp. Pure silica microspheres post-synthetically impregnated with tungsten were prepared as follows: a mixture of 50 mL *N*,*N*′-dimethylformamide (DMF), 0.5 mL ultra-pure water (UPW), and 0.5 mL absolute ethanol was placed in a Teflon container. Subsequently, 496.6 mg of 2,6-naphthalenedicarboxylic acid (H_2NDC) was added, and the container was sealed and placed in a microwave reactor (ERTEC Magnum II; 600 W; 2.45 GHz). The microwave power was set to 70% (420 W), and the reaction mixture was heated to 180 °C for 40 minutes under microwave irradiation. After cooling to room temperature, the transparent NDC precursor solution was slowly added to a stirred solution of (3-aminopropyl)triethoxysilane (APTES, 2.30 g, 10.39 mmol) in 70 mL DMF. A white precipitate formed immediately, and the mixture was stirred at room temperature for 4 hours. The precipitate was separated by centrifugation (6000 rpm, 5 minutes) and dried in an oven at 80 °C overnight, yielding 1.234 g of the NDC–Si solid precursor. Next, the NDC–Si precursor was calcined in air at 500 °C for 4 hours (heating rate: 5 °C min^{-1}) to remove the NDC linker, producing 403 mg of silica-based material. Subsequently, 385 mg of this silica material was mixed with ammonium metatungstate hydrate (70.2 mg) dissolved in 5 mL demineralized water. The mixture was dried at 80 °C under continuous stirring, and the resulting slurry was calcined in a muffle furnace at 550 °C for 3 hours (heating rate: 5 °C min^{-1}) in air. The tungsten content in the final sample (4W–SiO_2-imp) was determined to be 4.1 ± 0.1 wt% according to ICP-OES.

2.1.4 Ethanol dehydration. A fixed-bed catalytic reactor connected to a gas chromatograph with a flame ionization detector was used for the catalytic reaction. The catalytic tests were performed at temperatures of 300, 330, 360, 390 and 420 °C. One temperature step consisted of (i) a heating ramp (5 °C min^{-1}) and stabilization at the set temperature (20 min) and (ii) a steady temperature state (60 min at 300 and 330 °C; 84 min at 360, 390, and 420 °C). The analysis of the effluent gas and the evaluation of ethanol dehydration activity were carried out by using an HP 6890 Gas Chromatograph (five injections at each temperature) equipped with a flame ionization detector (FID) and an Agilent J&W HP-PLOT/G GC column (30 m long, internal diameter of 0.32 mm, film thickness of 20 μm). The stability experiments were carried out for 12 h at 420 °C. Calcined catalysts (50 mg) mixed with 50 mg of chromatographic silica were used for the catalytic reaction. The void space of the reactor was filled with silica beads. Before the reaction, the catalysts were pre-treated in nitrogen for 1 h at 300 °C. Nitrogen was used as the carrier gas (50 cm^3 min^{-1}); ethanol was fed by a NE-300 syringe pump with a WHSV of 14.19 h^{-1} (7.09 h^{-1} in a specific case). In addition, the setup with the carrier gas co-fed with 20% O_2 (10 mL O_2 and 40 mL N_2) was used in the stabilization studies. Pentane (5% molar concentration in ethanol feed) was used as an internal standard. The tests were carried out at atmospheric pressure.

2.2 Characterization techniques

2.2.1 Elemental analyses. The content of tungsten and silicon elements in the W–SiO_2 samples was determined by ICP-OES performed on an iCAP PRO XPS Duo spectrometer (tungsten spectral lines $\lambda = 224.875$ and 239.709 nm; silicon spectral line $\lambda = 250.690$ nm). The samples were mineralized with HNO_3 and HF.

2.2.2 XRD analysis. Powder X-ray diffraction (XRD) patterns of the W–SiO_2 microspheres were collected using a Rigaku MiniFlex 600 diffractometer equipped with a Co Kα radiation source (λ = 1.7903 Å, 40 kV, 15 mA). The resulting data were processed with Rigaku PDXL2 software.

2.2.3 Thermal analysis. Thermogravimetric analyses were performed on a Setaram LabSys Evo instrument with a TG/DSC sensor in an air atmosphere (airflow 60 cm^3 min^{-1}), at a heating rate of 5 °C min^{-1}, in the temperature range of 30–1000 °C.

2.2.4 Solid-state NMR spectroscopy. ^{13}C CP TOSS, ^{13}C and ^{29}Si solid-state NMR spectra were measured on a Bruker Avance III HD 700 MHz spectrometer with a MAS DVT 700S4 BL4 N-P/H probe. Chemical shifts were referenced externally to ^{29}Si δ [$(Me_3SiO)_8Si_8O_{20}$]: 11.72 ppm; ^{13}C δ [adamantane]: 38.68 ppm. The ^{13}C CP TOSS MAS NMR spectrum was measured with a spinning rate of 5 kHz. The ^{13}C MAS NMR spectrum was recorded at a 12 kHz spinning rate and d1 of 100 s. ^{29}Si MAS NMR was measured with a spinning rate of 12 kHz.

2.2.5 Infrared and Raman spectroscopy. The FTIR spectra of the W–NDC–Si-based solid precursor and W–SiO_2 microspheres were recorded on a Thermo Nicolet 6700 spectrometer using an ATR technique with a diamond crystal (resolution 2 cm^{-1}, 4000–400 cm^{-1}). Raman spectra were acquired using

a Thermo Nicolet DXR Raman microscope equipped with a laser operating at an excitation wavelength of 780 nm. Spectral data were collected in the range of 2000 to 50 cm^{-1} under standard ambient conditions.

2.2.6 UV-vis spectroscopy. The DRUV-vis measurement was carried out on a UV-Vis spectrometer PerkinElmer Lambda 1050 equipped with a 150 mm integration sphere with a InGaAs photodetector. The samples were prepared by drying the powder product in a vial flask in a vacuum oven at 150 °C for 3 hours. After drying, the samples were flushed with nitrogen and immediately transferred to a UV-vis powder cell (UV-Vis-NIR Powder Cell Kit, Agilent). Diffuse reflectance measurements were converted to absorbance using the Kubelka–Munk function.[40] The edge energy for direct allowed transitions was estimated by using the Tauc plot.

2.2.7 X-ray photoelectron spectroscopy. X-ray photoelectron spectroscopy (XPS) measurements were performed using a Kratos Analytical Axis Supra spectrometer equipped with monochromatized Al-Kα radiation (1486 eV). Sample powders were deposited onto double-sided copper tape affixed to the sample holder. The analysis chamber pressure was maintained at approximately 10^{-6} Pa. The analyzed area was about 1.4 mm^2, with the pass energy set to 150 eV. The binding energy scale was calibrated by setting the C 1s peak of carbon to 284.8 eV.[41] Data treatment was performed with the CasaXPS program (Casa Software Ltd, UK), and spectra were deconvoluted with the least-squares fitting routine provided by the software with a Gaussian/Lorentzian (85/15) product function after subtraction of a nonlinear baseline.[42] W 4f spectra were fitted with a $4f_{7/2}$–$4f_{5/2}$ doublet separation of 2.18 eV and with area ratios of 4 : 3. The W4f – $4f_{7/2}$ and $4f_{5/2}$ peaks were generally all constrained to have an equal FWHM.

2.2.8 Microscopy. Scanning electron microscopy (SEM) was conducted using a Nova NanoSEM (FEI) operated at 5 kV, equipped with a Schottky field emission gun (FEG) electron source and a TLD secondary-electron detector. SEM energy-dispersive X-ray (EDX) analyses were performed with an Octane Plus EDX spectrometer (EDAX, AMETEK, Inc.) featuring a SDD detector. Scanning transmission electron microscopy energy-dispersive X-ray spectroscopy (STEM-EDS) was carried out on a Thermo Fisher Scientific Talos F200C instrument equipped with a Bruker Xflash 6T-30 detector, operating at 200 kV. STEM imaging utilized a high-angle annular dark-field (HAADF) detector to provide atomic *Z*-contrast. For STEM-EDS analysis, the powder sample was dispersed in hexane, and 4 μL of the suspension was deposited onto a QuantiFoil R 2/2 200 mesh copper grid, followed by drying at ambient temperature. The sample was subsequently plasma-cleaned for 80 s in a low-pressure H_2/O_2 atmosphere using a Gatan Solarus II system to minimize organic contamination.

2.2.9 Nitrogen adsorption/desorption porosimetry and water vapor sorption. Nitrogen adsorption–desorption isotherms were measured at 77 K using a BELsorp Mini II instrument (Japan). Prior to analysis, the samples were degassed in the BELsorp preparation unit at 300 °C for 20 hours. The specific surface area was determined by the multi-point Brunauer–Emmett–Teller (BET) method, utilizing at least five data points within the relative pressure range of 0.05 to 0.30.[43] The total pore volume was measured at $p/p_0 = 0.99$. Pore size distributions were calculated using the NLDFT method and adsorption branch of isotherms.[44] To measure water vapor sorption at 298 K, a BELsorp MAX X instrument was used. Water was taken from a Milli-Q system. The water was degassed in the BELsorp MAX X instrument by repeated freezing cycles using liquid nitrogen followed by high vacuum application according to the recommended procedure by Belsorp. Temperature of the samples was maintained at 298 ± 0.1 K by use of a circulating water bath.

2.2.10 Water contact angle. Water contact angles were measured using a See System E (Advex Instruments). For this analysis, samples were prepared in the form of pellets. A 5 μL droplet of water was deposited onto the sample surface.

2.2.11 Time of flight secondary ion mass spectrometry (ToF-SIMS). Chemical characterization of W–SiO_2 samples was carried out by using a ToF-SIMS^5 instrument (IONTOF GmbH, Münster, Germany). A pulsed Bi_5^+ metal ion source generated the primary ion beam at an acceleration voltage of 30 kV. An AC target current of 0.08 pA with a bunched pulse width lower than 1 ns was used. Both positive and negative secondary ion species were analyzed. Spectra were acquired over a raster of 128 × 128 data points across a 300 × 300 μm^2 area. To maintain static conditions, the total primary ion dose per unit analyzed area was kept below 3×10^{10} ions per cm^2. The lateral resolution of ~3 μm and mass resolution $m/\Delta m$ > 4000 at 29 m/z were maintained for positive and negative spectrum acquisition. Charge compensation was done by an interlaced electron flood gun (E_k = 20 eV). All data were processed using SurfaceLab software (version 6.8), supplied by the instrument manufacturer. Sample powders were mounted by pressing them onto the adhesive surface of Post-it® notes. The data for each sample were recorded from three different spots on the surface.

3 Results and discussion

3.1 Catalyst characterization

In this work, a novel sol–gel synthetic procedure for W–SiO_2 microspheres is introduced and their catalytic activity in alcohol dehydration is demonstrated. The fine dispersion of tungstate species in microspheres was achieved through a preparation technique involving the microwave-assisted heating of $W(CO)_6$ and 2,6-naphthalene dicarboxylic acid precursors, followed by condensation with APTES. Within this procedure hybrid metallosilicate solid precursors (Fig. 1a) with different W loadings were prepared (FTIR and TGA analyses of 12W–NDC–Si are given in SI; Fig. 2S and 3S) and, after subsequent calcination at 550 °C, they were transformed to inorganic W–SiO_2 materials (Fig. 1b) containing 2, 6, and 12 wt% of W. The described synthesis was inspired by our previous work on Mo–SiO_2 and V–SiO_2 microspheres, which have exhibited highly homogeneous metal dispersions and outstanding catalytic activities in olefin metathesis, olefin epoxidation, and ethyl lactate oxidation.[37–39] However, here we have applied a different linker: previously applied 4,4′-biphenyl dicarboxylic acid has been replaced by cost-effective 2,6-naphthalene dicarboxylic

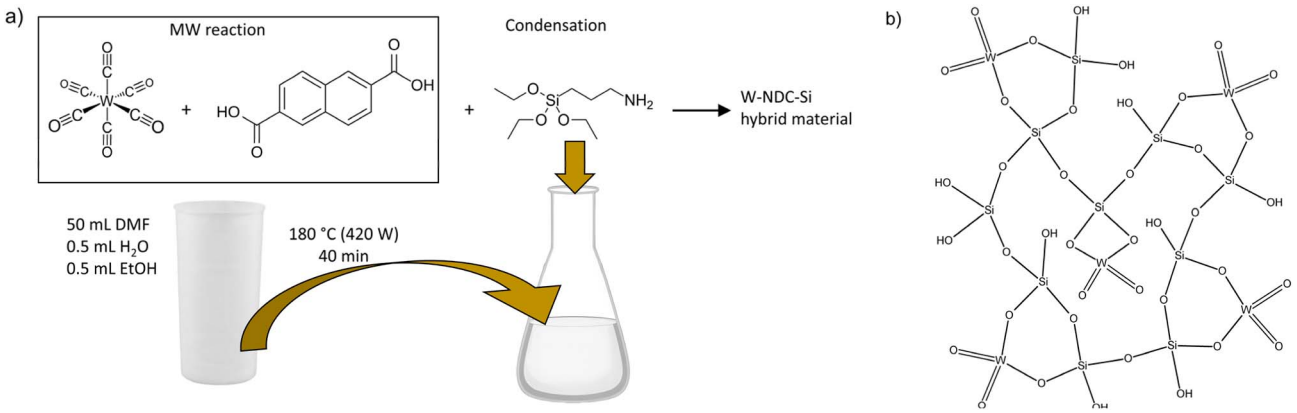

Fig. 1 (a) Reaction procedure scheme. (b) Proposed structural motif of W–SiO_2 microspheres.

acid. For the sake of comparison, the pure SiO_2 microspheres prepared *via* the same methodology were impregnated with ammonium metatungstate hydrate. This sample is labeled as 4W–SiO_2-imp.

Solid-state NMR spectroscopy was used to identify functional groups in both the as-prepared (12W–NDC–Si) and calcined (12W–SiO_2) samples. This experiment was performed to confirm the elimination of ethoxy groups during the sol–gel condensation. The ^{13}C TOSS CPMAS and ^{13}C MAS NMR spectra are shown in Fig. 2a. The signals for different functional groups are distinguishable. The carbon atoms from the 3-aminopropyl group appear at 14, 25, and 46 ppm. Since the signals of ethoxy groups from APTES did not significantly appear in the ^{13}C TOSS CPMAS NMR spectrum, it can be concluded that ethoxy groups are released in the form of ethanol as the product of the condensation between APTES and W–NDC species in the precursor solution. The NDC linker is identified by distinct carbonyl resonance observed at 176 ppm. Additionally, the ^{13}C MAS NMR spectrum was recorded as well (Fig. 2a). As expected, the intensity of signals originating in the NDC linker is increased compared to the ^{13}C TOSS CPMAS NMR spectrum due to the absence of signal intensity enhancement *via* cross-polarization. The ratio between the aminopropyl groups and the aromatic rings (from the linker) is approximately 1 : 0.87. This corresponds to a Si : NDC molar ratio of 1.15 : 1 in 12W NDC Si. This value is consistent with the mass losses recorded within the TGA analysis of 12W NDC Si (Fig. 3S).

The ^{29}Si MAS NMR spectrum of the 12W–NDC–Si sample is shown in Fig. 2b. The spectrum displays signals at chemical shifts of −60 and −67 ppm, corresponding to T^2 and T^3 type groups, respectively. In this case the T^2 type is attributed to $LSi(OR)(OSi)_2$ and T^3 type is characteristic of $LSi(OSi)_3$ species, where L: aminopropyl group, and R: W or NDC linker. The results confirm the condensation of APTES and are consistent with the findings from the ^{13}C TOSS CPMAS NMR analysis. Additionally, the ^{29}Si MAS NMR spectrum of the 12W–SiO_2 sample, shown in Fig. 2b, revealed signals corresponding to Q^n sites in silicates. This demonstrates the successful conversion of organosiloxanes into fully inorganic silicates after the calcination of 12W–NDC–Si. The features denoted as Q^4, Q^3, and Q^2

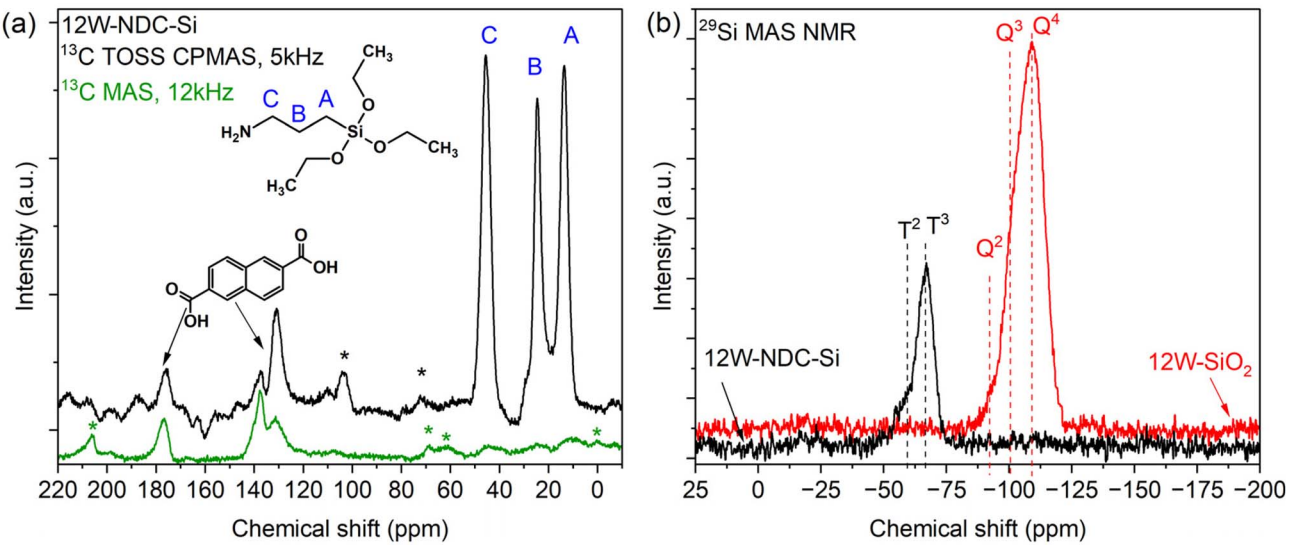

Fig. 2 ^{13}C TOSS CPMAS and ^{13}C NMR spectra of the 12W–NDC–Si sample (a). ^{29}Si MAS NMR spectra of 12W–NDC–Si and 12W–SiO_2 samples (b). Rotational sidebands are marked with an asterisk.

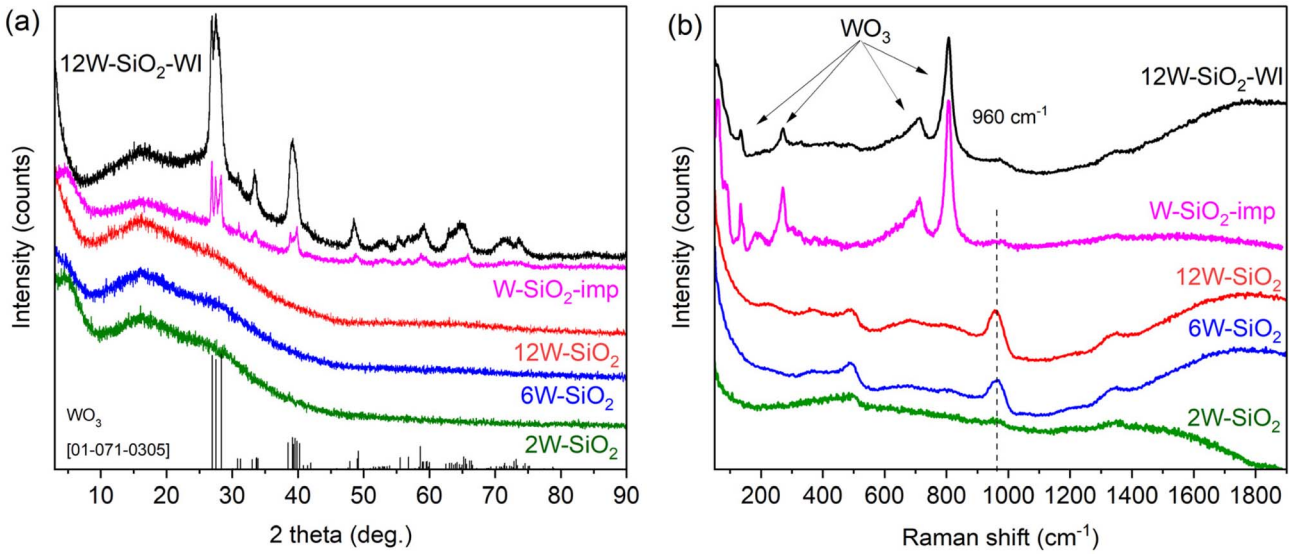

Fig. 3 PXRD diffractograms of W–SiO_2 microspheres (a). Raman spectra of W–SiO_2 microspheres (b).

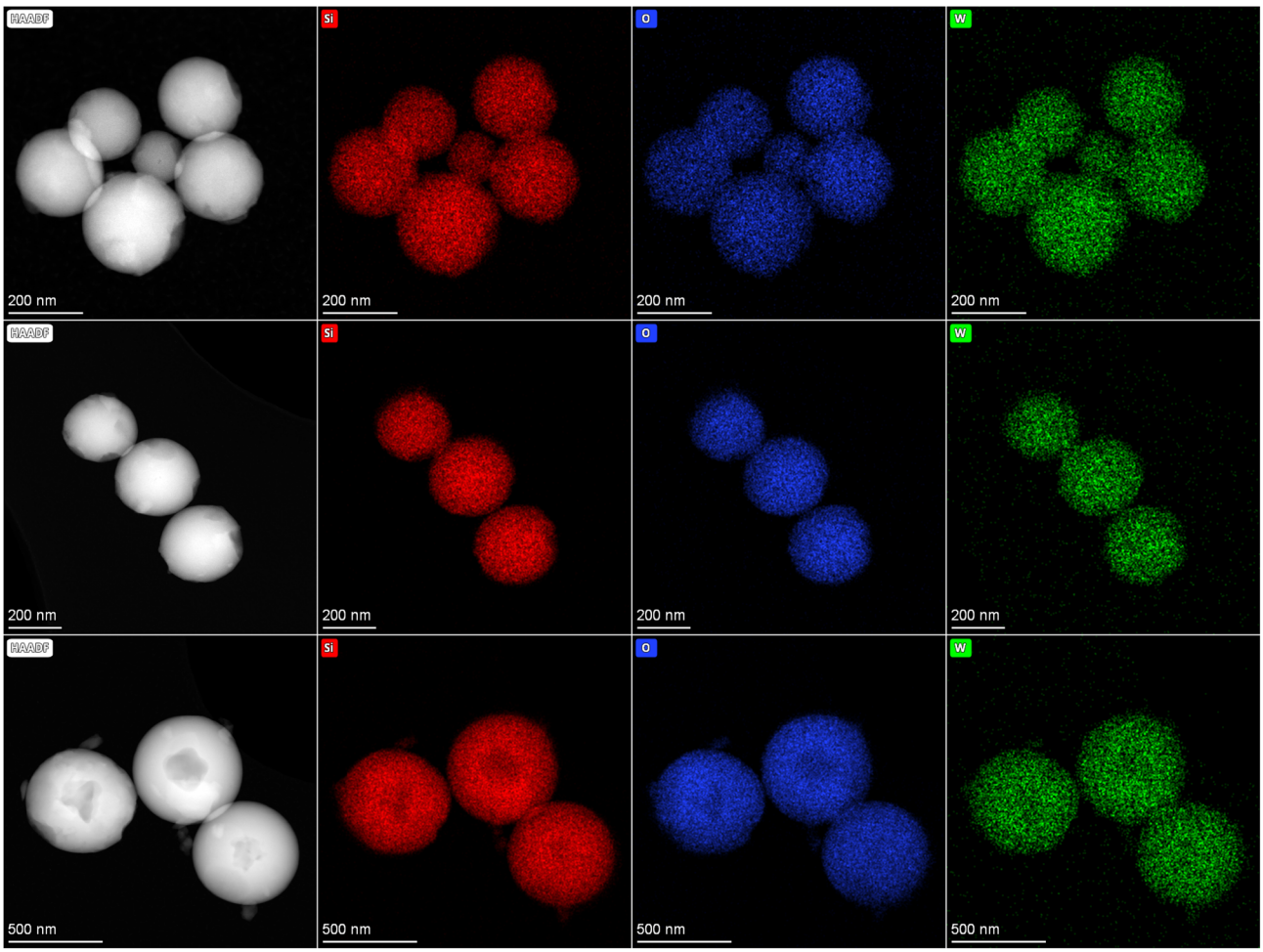

Fig. 4 HAADF images and STEM-EDS elemental maps of W–SiO_2 microspheres (12W–SiO_2 – upper row, 6W–SiO_2 – middle row, and 2W–SiO_2 – bottom row). Si – red, O – blue, and W – green.

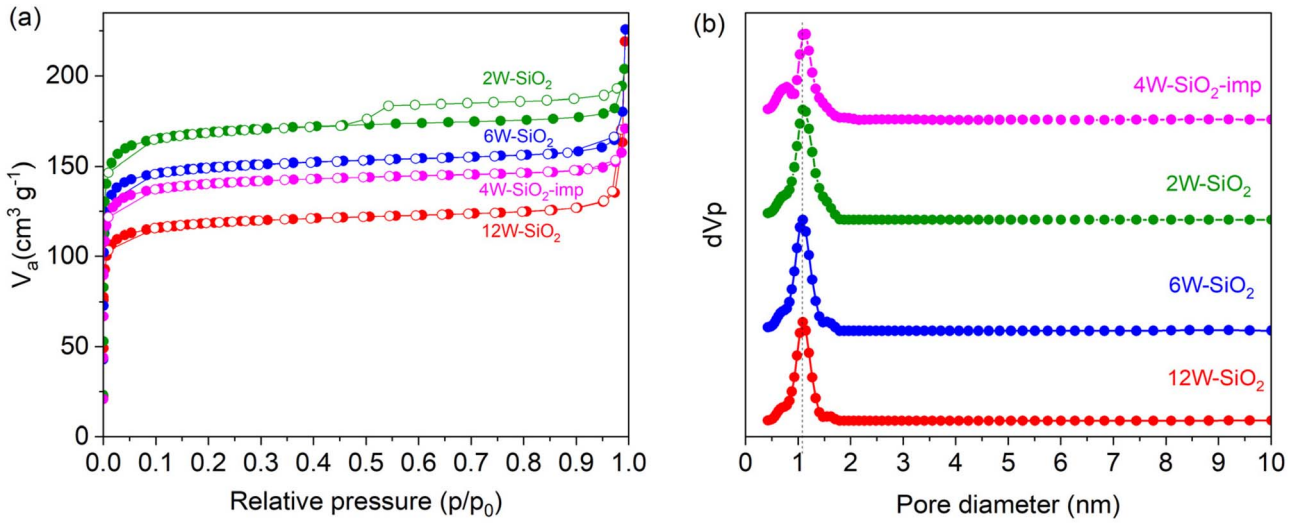

Fig. 5 Nitrogen adsorption/desorption isotherms of W–SiO_2 microspheres (a). Pore size distribution according to the NLDFT method (b).

correspond to the signals of $Si(OSi)_4$, $(WO)Si(OSi)_3$/HO–$Si(OSi)_3$, and $(WO)_2Si(OSi)_2$/$(HO)_2Si(OSi)_2$ species, respectively. As anticipated, because the MAS NMR spectra were acquired without using cross-polarization, the Q^4 sites (−110 ppm) exhibited the strongest signal intensity. The peaks corresponding to Q^3 (WO) $Si(OSi)_3$/HO–$Si(OSi)_3$ and Q^2 $(WO)_2Si(OSi)_2$/$(HO)_2Si(OSi)_2$ environments appeared at −101 ppm and −92 ppm, respectively.[24]

It was found that all W–SiO_2 microspheres are amorphous, showing no diffraction lines of WO_3 in their powder X-ray diffraction patterns (Fig. 3a). Moreover, Raman spectra of W–SiO_2 microspheres (Fig. 3b) did not show the presence of the bands indicating WO_3 crystalline species and therefore, the presence of the WO_3 crystalline phase can be safely excluded.[32,45] The band with a Raman shift of 960 cm^{-1} may be ascribed to the W=O bond.[46] It should be noted that in the case of supported WO_x/SiO_2 catalysts, separation of WO_3 oxide occurs already at a tungsten content of around 8–10 wt%.[32] However, our preparation technique can maintain the amorphous form of the tungstate species even for the microsphere sample with 12 wt% of tungsten. In contrast, the impregnated pure silica microspheres (4W–SiO_2-imp) and the 12W–SiO_2–WI sample prepared *via* the impregnation technique shows the presence of crystalline WO_3 in the PXRD diffractogram (JCPDS card no. 01-071-0305) and Raman spectrum (Fig. 3b).[18,32,47] These results demonstrate that the method, which integrates microwave-assisted heating with one-step sol–gel condensation, yields samples containing a high population of amorphous and well-dispersed tungstate species.[45]

Electron microscopy was employed to study the morphology of the W–SiO_2 samples derived from W–NDC–Si solid precursors and 4W–SiO_2-imp microspheres prepared *via* impregnation of pure silica microspheres. As illustrated by SEM (Fig. 4S–7S), all samples exhibited well defined spherical morphology. The average size of microspheres determined *via* graphical analysis of the SEM images was 265 ± 39 nm for 12W–SiO_2, 385 ± 38 nm for 6W–SiO_2, and 659 ± 33 nm for 2W–SiO_2 (Fig. 8S). It can be argued that the dispersion of tungsten in this kind of heterogeneous catalyst plays an important role in the catalytic activity. Therefore, the elemental distribution of silicon, tungsten, and oxygen in microspheres was investigated by STEM-EDS. Fig. 4 unambiguously shows that tungsten is homogeneously dispersed throughout the microspheres. Conversely, the STEM-EDS images of the 4W–SiO_2-imp sample (Fig. 9S) show an inhomogeneous dispersion of tungsten species and their agglomeration into larger particles, which is consistent with the PXRD and Raman spectroscopy results.

Nitrogen adsorption/desorption isotherms of W–SiO_2 microspheres are displayed in Fig. 5a (and in the case of the

Table 1 W–SiO_2 microsphere characteristics

Sample	W[a] [wt%]	SA(BET) [m^2 g^{-1}]	Pore volume [cm^3 g^{-1}]	Pore diameter [nm]	Microsphere diameter[b] [nm]	W surface density[c/d] [W nm^{-2}]
2W–SiO_2	1.96 ± 0.01	594	0.31	1.1	659 ± 33	0.05/0.10
6W–SiO_2	6.46 ± 0.01	512	0.30	1.1	385 ± 38	0.18/0.41
12W–SiO_2	11.83 ± 0.01	416	0.28	1.1	266 ± 39	0.62/0.93
4W–SiO_2-imp	4.01 ± 0.01	498	0.25	1.1	684 ± 129	0.17/0.26

[a] Determined by the ICP-OES method. [b] Calculated from SEM images. [c] Surface density was calculated as the number of W atoms per square nanometer of the catalyst[21] using the W content determined by XPS. [d] Surface density was calculated as the number of W atoms per square nanometer of the catalyst[21] using the W content determined by ICP-OES.

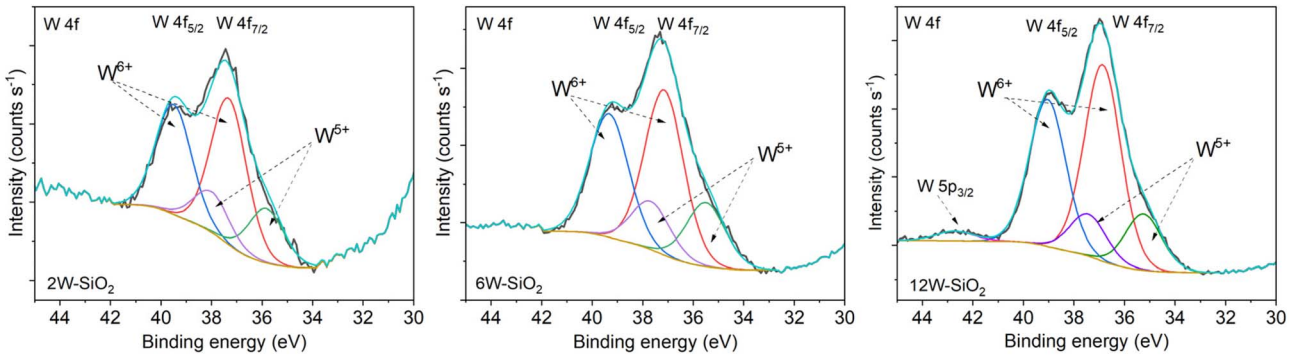

Fig. 6 W 4f XPS spectra of W–SiO_2 microspheres.

sample 12W–SiO_2–WI in the SI in Fig. 10S). According to the IUPAC classification, all isotherms of microspherical samples revealed a Type I shape that is indicative of microporous materials. Based on the BET method, high surface areas of 416, 512, and 594 $m^2\ g^{-1}$ were achieved for 12W–SiO_2, 6W–SiO_2, and 2W–SiO_2 microspheres (Table 1). The NLDFT method was used for pore size distribution calculation and confirmed a microporous character with a pore size distribution centered on a diameter of 1.1 nm for all samples (Fig. 5b). We attribute this behavior to the well-organized hybrid silicate framework crosslinked by the NDC linker, which, upon its removal during calcination, gives rise to the porous structure. SA and pore volume values, together with the tungsten contents and microsphere diameters, are listed in Table 1.

X-ray photoelectron spectroscopy (XPS) was employed to identify the tungsten oxidation state and functional groups on the surface of W–SiO_2 microspheres. Survey scans over the whole binding energy (BE) range are included in the SI (Fig. 11S). As illustrated in Fig. 6, the high-resolution W 4f spectra of W–SiO_2 microspheres revealed W $4f_{5/2}$ and W $4f_{7/2}$ contributions of the W^{6+} and W^{5+} valence states after deconvolution and fitting of the recorded data.[5,11,48] In the case of sample 12W–SiO_2, the W $4f_{5/2}$ and W $4f_{7/2}$ spin–orbit doublets of the W^{6+} and W^{5+} states appear at 39.0 and 36.8, and 37.5 and 35.3 eV, respectively. These positions align with published data on WO_x/SiO_2 catalysts.[5,25,47,48] In contrast, the W 4f spectrum of 12W–SiO_2–WI (Fig. 12S) shows W^{6+} contributions at 37.4 eV (W $4f_{5/2}$) and 35.3 eV (W $4f_{7/2}$), characteristic of bulk WO_3.[49] Specifically, shifts to higher binding energy regions in the tungsten 4f XPS peaks when WO_x is dispersed on silica compared to its bulk WO_3 form have been reported in several studies.[25,50–52] It is suggested that these shifts could be attributed to changes in electron density resulting from metal–support interactions. Furthermore, Howell *et al.* noted that the tungsten oxide dispersion on a silica support influences catalytic behavior and is reflected in shifts of the 4f peaks toward higher binding energies.[53] Thus, the observed high W $4f_{5/2}$ and W $4f_{7/2}$ binding energies indicate a well dispersed WO_x in W–SiO_2 microspheres in accordance with the other analyses (DRUV-Vis spectroscopy and STEM-EDS). XPS spectra of the 4W–SiO_2-imp sample are given in the SI (Fig. 13S and 14S).

Based on the XPS results the tungsten content on 12W–SiO_2, 6W–SiO_2, and 2W–SiO_2 microsphere surfaces is 7.9, 2.8, and 0.9 wt%, respectively (Table 2S), which is lower than the corresponding bulk contents determined by the ICP-OES method. This may be attributed to the more rapid polycondensation reactions occurring around tungsten centers during synthesis, which lead to a comparatively lower tungsten concentration on the surface than within the interior of the walls. Hence, the surface Si and O concentration is complementarily higher. O 1s high-resolution XPS spectra are given in the SI (Fig. 15S–17S). As illustrated, the contributions of W=O and Si–O species at a BE of 530.9 and 532.8 eV, respectively, are found in the spectra. Moreover, Si–OH and C–O moieties with a BE of 533.6 and 538.8 eV were evidenced. In the Si 2p high-resolution XPS spectra (Fig. 13S–15S), the characteristic contributions of Si–O–Si and Si–OH moieties were evidenced. Notably, the number of adsorbed species (adventitious carbon) on the catalyst surface is very low as expected (Fig. 11S, 15S–17S and Table 2S).

Time-of-flight secondary ion mass spectrometry (ToF-SIMS) offered detailed information on the tungstate species present at the outermost surface of the catalysts.[54–56] Table 3S lists all quantified W-containing secondary anions detected and identified during analysis. The overall proportion of W-containing clusters in the W–SiO_2-based microspheres (determined as the sum of the normalized intensities of each W-containing anion) logically increased with the W loading (Fig. 18S). At the same time, it can be seen that the 12W–SiO_2–WI sample prepared by the impregnation technique exhibits the highest proportion of tungsten clusters on the surface, as expected. Detected ions were categorized based on W nuclearity: (1) ions with one W atom (WO_3^-, WO_4^-, WO_5Si^-, and $WO_7Si_2^-$), and (2) ions with multiple W atoms ($W_2O_6^-$ and $W_3O_9^-$). The relative intensities of clusters with one W atom serve as a useful indicator of WO_x dispersion. Conversely, a high proportion of clusters with multiple W atoms suggests the presence of condensed species, such as poly-tungstates or crystalline WO_3. As illustrated in Fig. 7, the ratio of monomeric W-containing clusters to total counts of detected W-containing clusters was significantly higher in W–SiO_2 as compared to both 4W–SiO_2-imp and 12W–SiO_2–WI samples (Fig. 7). Noteworthily, ToF-SIMS shows that the proportion of highly dispersed WO_x species at the surface of the W–SiO_2 microspheres remains similar whatever the W

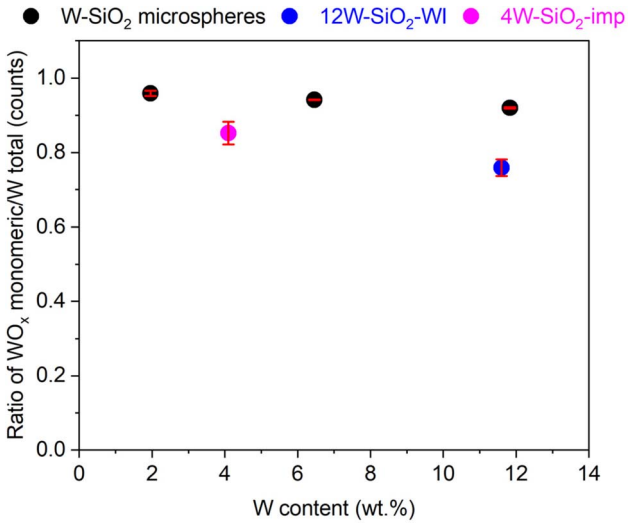

Fig. 7 The ratio of WO_x monomer clusters/all tungsten containing clusters on the W–SiO_2 catalyst surface by the ToF-SIMS technique. Error bars show the standard deviation of each data set (3 analyses per sample).

loading. Thus, ToF-SIMS showed a better W dispersion in W–SiO_2 samples in comparison to impregnated materials at the outermost surface of the tungsten silicates complementing the XPS, STEM-EDS, XRD, and Raman analyses.

Diffuse reflectance UV-vis spectroscopy was conducted in order to evaluate the local structure (isolated monomer, dimer, polymeric chain, cluster, or three-dimensional structure) of tungsten species *via* the ligand-to-metal charge transfer (LMCT) band position and the corresponding edge energy (E_g) value. DRUV-vis spectroscopy measurements (Fig. 8a) were performed on the samples dried under vacuum (150 °C, flushed with nitrogen). A distinctive characteristic of DRUV-vis spectra for isolated WO_4 reference compounds is the presence of a single ligand-to-metal charge transfer (LMCT) band in the range of approximately 218–274 nm, with most band maxima occurring between 220 and 250 nm. In contrast, bulk WO_3 displays two LMCT transitions at 251 nm and 338 nm.[45] The corresponding band edge energy values, E_g, for regular isolated WO_4 structures are 5.2–5.6 eV, whereas the energies of 4.0–4.5 eV are reported for the distorted WO_4 structures.[45,57] For example, Na_2WO_4, in which W is present as isolated tetrahedral centers exhibits E_g = 4.7 eV.[53] As demonstrated in Fig. 8b, the band edge values for 12W–SiO_2, 6W–SiO_2, and 2W–SiO_2 are 4.00, 4.10, and 4.58 eV. These values can support the presence of the distorted WO_4 species, especially for 12W–SiO_2 and 6W–SiO_2 microspheres. In the case of the 2W–SiO_2 sample, the sharp band in DRUV-vis spectra with a maximum at 215 nm and band edge value of 4.58 eV may be assigned to isolated WO_4 species.[32,45] The E_g value of the 4W–SiO_2-imp microspherical sample was 3.92 eV, lower than that of all W–SiO_2 samples, a hint of worse dispersion of tungsten species in samples prepared *via* impregnation. The position of the maxima in the DRUV-vis spectra suggests the presence of a certain proportion of dispersed tungstate species. However, significant absorption in the 320–450 nm region (Fig. 8a) demonstrates a poorer distribution of tungsten in this sample, further supported by PXRD, Raman, and STEM-EDS analyses. In the case of the 12W–SiO_2–WI sample, the band is shifted to a significantly higher wavelength indicating poor tungsten dispersion and the presence of tungsten oxide species (in agreement with XRD and Raman spectroscopy). Accordingly, the band edge energy reaches 3.34 eV, which corresponds to isopolytungstate species containing WO_6 clusters—consistent with literature values reported between 3.0 and 3.6 eV.[11,45]

Pyridine adsorption tests were performed to investigate the surface acidity of W–SiO_2 microspheres. Pyridine was adsorbed on dried samples (150 °C, vacuum), and acid sites were monitored by FTIR spectroscopy. As illustrated in Fig. 9, all W–SiO_2 microspheres contain both Lewis and Brønsted acid sites characterized by vibrational bands at 1449 and 1545 cm^{-1}, respectively.[11,58] Both types of sites have been shown to be active

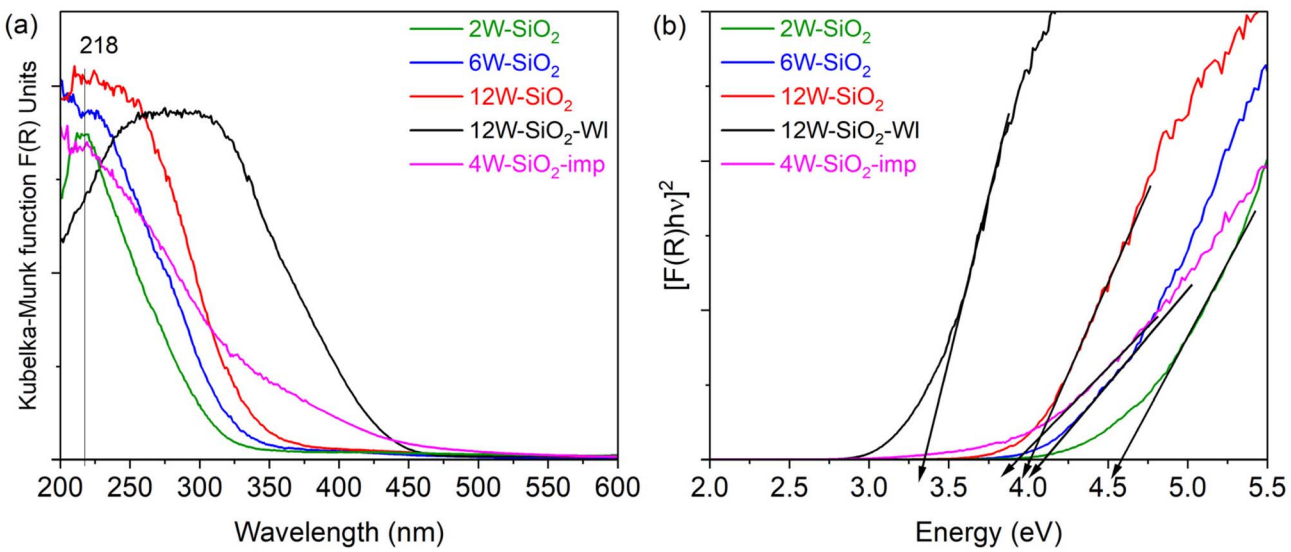

Fig. 8 Diffuse reflectance UV-vis spectra of W–SiO_2 microspheres (a) and Tauc plots with band edge energy values (E_g) (b).

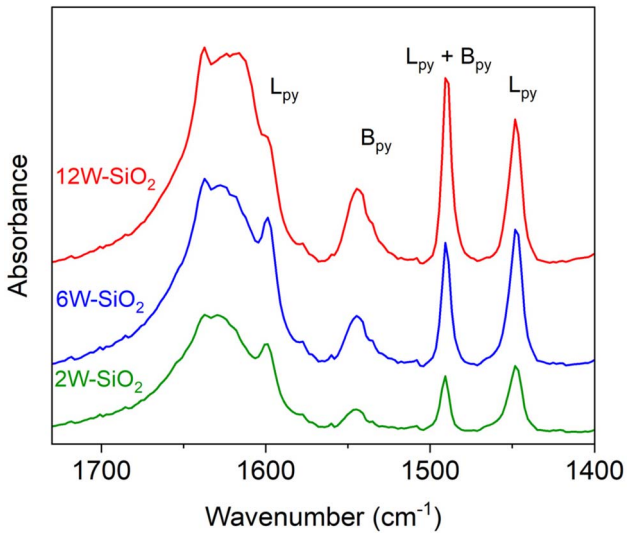

Fig. 9 FTIR spectra of 12W–SiO_2, 6W–SiO_2, and 2W–SiO_2 catalyst samples after the adsorption of pyridine (left). TG and dTG curves of 12W–SiO_2, 6W–SiO_2, and 2W–SiO_2 catalyst samples after the adsorption of pyridine.

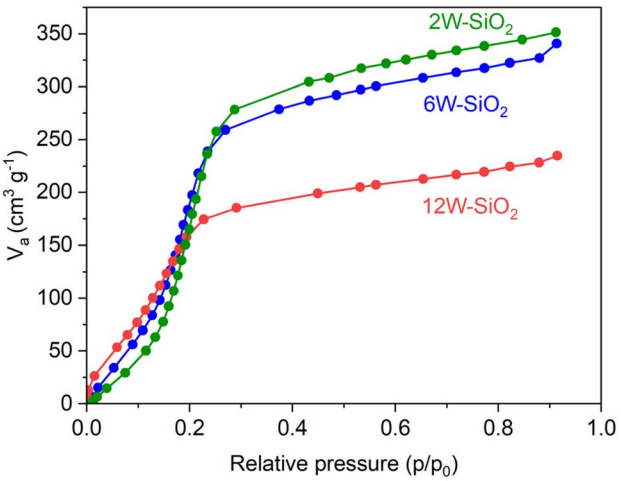

Fig. 10 Water vapor adsorption isotherms of W–SiO_2 microspheres.

in ethanol dehydration. Specifically, Lewis sites, characterized by tungsten di-oxo species, help stabilize reaction intermediates and participate in the elimination mechanism, while Brønsted sites are responsible for the protonation of ethanol.[26–28,59,60]

The L_{py} (1449 cm^{-1}) and B_{py} (1545 cm^{-1}) bands were deconvoluted and integrated, and the L_{py}/B_{py} ratio was calculated taking into account the integrated molar extinction coefficients (IMECs) reported by Emeis,[61] Zholobenko,[62] and Gallo[63] for silica–alumina-based catalysts. The IMEC values used for pyridine adsorbed on Lewis and Brønsted acid sites were 2.22 and 1.67 cm μmol^{-1}, respectively. The absorption band areas for pyridine adsorbed on Lewis and Brønsted acid sites, along with the L_{py}/B_{py} area ratios, are presented in Table 2. Based on these data, it can be concluded that the 12W–SiO_2 catalyst (L_{py}/B_{py} = 0.95) exhibited a significantly higher population of Brønsted acid sites compared to the 6W–SiO_2 and 2W–SiO_2 microspheres. Conversely, the L_{py}/B_{py} ratios of 1.50 and 2.00 obtained for 6W–SiO_2 and 2W–SiO_2, respectively, indicate a higher population of Lewis acid sites.

For deeper insights, TG analysis of the samples with adsorbed pyridine was performed in a nitrogen atmosphere. As illustrated in Fig. 19S, the mass losses assigned to pyridine desorption are observed at temperatures above 160 °C. According to the derivatives of the TG curves, the mass loss attributed to the adsorbed pyridine was evidenced. The amount of pyridine adsorbed on 12W–SiO_2, 6W–SiO_2, and 2W–SiO_2 catalysts, determined by TG analysis, reached 4.54, 3.66, and 2.04 wt%, respectively (Table 2), which corresponds to the tungsten content in the samples. The pyridine adsorption study for the 12W–SiO_2–WI and 4W–SiO_2-imp samples is presented in the SI (Fig. 20S). A noticeably lower intensity of absorption bands associated with the Lewis acid sites is observed compared to the microspherical W–SiO_2 samples. Additionally, thermogravimetric (TG) analysis indicates a pyridine mass loss of 1.27% for 12W–SiO_2–WI (0.16 mmol g^{-1} of pyridine), the lowest among all W–SiO_2 samples prepared herein. TGA analysis of the 4W–SiO_2-imp sample after pyridine adsorption (Fig. 20S) exhibited mass loss in the region of 160–290 °C corresponding to 3.1 wt% (0.39 mmol g^{-1}) of pyridine (Table 4S). Interestingly, when comparing the dTG curve of 4W–SiO_2-imp-py with the dTG curves of W–SiO_2-py microspheres, the maxima are found at 236 and 247 °C, respectively, indicating that pyridine is released at slightly higher temperatures in the case of W–SiO_2 microspheres prepared *via* the condensation approach, which may suggest a stronger interaction between pyridine and these microspheres.

In conjunction with the TG analysis of pyridine-adsorbed samples, the populations of Lewis and Brønsted acid sites can be correlated with the observed mass loss (Fig. 19S). According to the L_{py}/B_{py} ratios derived from FTIR, the quantities of L_{py} and

Table 2 The L_{py}/B_{py} ratios derived from FTIR and the quantities of L_{py} and B_{py} sites derived from TGA and FTIR

	Pyridine mass loss						
Catalyst sample	TG [%]	L_{py} area[a]	B_{py} area[a]	L_{py}/B_{py}[a]	Pyridine [mmol g^{-1}]	L_{py} [mmol g^{-1}]	B_{py} [mmol g^{-1}]
12W–SiO_2-py	4.54	4.43	4.67	0.95	0.57	0.28	0.29
6W–SiO_2-py	3.66	4.46	2.98	1.50	0.46	0.28	0.19
2W–SiO_2-py	2.04	2.31	1.15	2.00	0.26	0.17	0.09

[a] IMEC taken into account.[61–63]

B_{py} sites are summarized in Table 2. For example, the 12W–SiO_2 catalyst contained 0.29 mmol g^{-1} of B_{py} sites, whereas the 2W–SiO_2 sample contained only 0.09 mmol g^{-1}. Furthermore, the L_{py} content in 12W–SiO_2 was 0.28 mmol g^{-1}, while the 2W–SiO_2 sample exhibited 0.17 mmol g^{-1}.

To evaluate the hydrophilic or hydrophobic character of the W–SiO_2 microspheres, water vapor sorption measurements were performed.[35,64–66] The resulting adsorption isotherms are presented in Fig. 10 and, according to the IUPAC classification, exhibit a Type V profile. All isotherms display a steep increase in adsorption at low relative pressures, which is characteristic of hydrophilic materials.[66] Moreover, the individual W–SiO_2 microsphere samples differ in the specific relative pressure range at which water uptake occurs. As illustrated in Fig. 10, for the 12W–SiO_2 sample, water uptake begins at the lowest relative pressure (p/p_0). As the tungsten content decreases, the onset of the steep adsorption shifts toward higher p/p_0 values. This trend indicates that 12W–SiO_2 exhibits a more hydrophilic character compared to 6W–SiO_2 and 2W–SiO_2.[35,67,68] The values of water volume adsorbed on the W–SiO_2 microsphere surface corresponds with the nitrogen adsorption/desorption isotherms (Fig. 5).

The results from water sorption experiments correlate with the water contact angles measured on the surface of W–SiO_2 microspheres in the form of pellets. As illustrated in Fig. 21S, the water contact angle decreases with increasing tungsten content. The values for 2W–SiO_2, 6W–SiO_2, and 12W–SiO_2 were 38.9, 29.6, and 13.3°, respectively. Due to high hydrophilicity, the quality of the drop captured on the surface of the 12W–SiO_2 sample is poor.

3.2 Catalytic studies

The potential application of W–SiO_2 microspheres in catalysis was demonstrated on ethanol dehydration to ethylene. First, the ethanol dehydration reactions were performed at two different WHSV values (14.19 and 7.09 h^{-1}) to check the occurrence of a mass transfer limitation (Fig. 22S). As illustrated, the initial conversion doubled when WHSV was decreased to 7.09 h^{-1}.[69] Also, Weisz–Prater and Mears criteria were well below 0.3 and 0.15, respectively, excluding possible mass transfer limitations (Tables 5S and 6S). Thus, catalytic studies were performed at 14.19 h^{-1} to ensure that conversion is well below 100% (*i.e.*, under the kinetic regime).[70,71]

The average ethanol conversions and ethylene selectivity from each five injections at the temperatures of 300–390 °C (Fig. 11a) are given in SI (Fig. 23S). As illustrated in Fig. 11a, the conversion of ethanol increased with temperature, reaching the highest initial conversion of 43% at 420 °C for the 12W–SiO_2 sample. However, the 12W–SiO_2 sample exhibited significant deactivation over time on stream (TOS), primarily due to coking, as discussed later. For the 6W–SiO_2 and 2W–SiO_2 catalysts, which have lower tungsten loadings, the conversion at 420 °C was 31% and 24%, respectively. These samples showed better stability with less prominent deactivation compared to the 12W–SiO_2 sample.

The initial ethylene selectivity was fluctuating close to 100% for the 12W–SiO_2 sample. Although ethylene selectivity decreased (in favor of acetaldehyde[72]) over time-on-stream (from 100% to 65% in 14 h), it remained higher than that of the 6W–SiO_2 and 2W–SiO_2 microspheres (Fig. 11c). Trace amounts of diethyl ether were detected across all samples, regardless of tungsten loading or reaction temperature; however, its selectivity remained negligible (<1%).

The high potential of W–SiO_2 microspheres for ethanol dehydration is further demonstrated in Fig. 11b, which shows the initial ethylene productivity. The 12W–SiO_2 sample achieved the highest initial ethylene productivity of 132.6 mmol g^{-1} h^{-1}. With time on stream, however, ethanol conversion decreases and acetaldehyde selectivity increases. 6W–SiO_2 and 2W–SiO_2 samples with initial ethylene productivities of 80.2 and 55.6 mmol g^{-1} h^{-1}, respectively, exhibited more stable ethanol conversion, so that the ethylene productivity across all catalyst samples plateaued at nearly the same value (25 mmol g^{-1} h^{-1}) after 17 h TOS. A high initial ethylene productivity in the 12W–SiO_2 catalyst can be ascribed to the high concentration of Brønsted acid sites as the initial ethylene productivities for 2W–SiO_2, 6W–SiO_2, and 12W–SiO_2 samples correlate with the number of Brønsted acid sites (Table 2 and Fig. 24S).

The results obtained for W–SiO_2 catalysts prepared by the microwave-assisted sol–gel technique contrast with the catalytic performance of the 12W–SiO_2–WI catalyst prepared by the wet impregnation technique, which simulates an industrial catalyst. 12W–SiO_2–WI reached only 10% ethanol conversion, with ethylene selectivity dropping rapidly over time on stream from ~80 to 20% in parallel with an increase in acetaldehyde selectivity. Overall, maximum productivity of 12W–SiO_2–WI reached only 21 mmol g^{-1} h^{-1} at 420 °C with a decreasing trend during TOS (6 mmol g^{-1} h^{-1} after 14 h) (Fig. 11b). Similarly, the 4W–SiO_2-imp sample prepared *via* impregnation of pure silica microspheres synthesized *via* MW-assisted sol–gel technique exhibited lower initial ethanol conversion (17%) at 420 °C as well as lower initial ethylene productivity (43 mmol g^{-1} h^{-1}) than W–SiO_2 microspheres prepared *via* the one-pot approach (Fig. 11). Similarly, the ethylene productivity decline during TOS was evidenced resulting in a value of 11 mmol g^{-1} h^{-1}, after 12 h (Fig. 11c). Interestingly, this sample shows relatively high and stable selectivity to ethylene.

Clearly, the well-dispersed active sites in W–SiO_2 microspheres play a crucial role in achieving high catalytic activity as shown by a correlation between initial ethylene productivity normalized to the tungsten molar content and DRUV-vis band-edge energy (Fig. 25S). Samples prepared *via* impregnation exhibited lower band-edge energies and lower ethylene productivities than W–SiO_2 catalysts prepared in one-pot. The tungsten surface density does not appear to be decisive (Fig. 25S).

If we normalize the activity of the catalysts to the molar content of tungsten (Fig. 26S), it is obvious that the space-time yield of ethylene is the highest in the case of the sample with the lowest tungsten content (520 mmol $mmol_W^{-1}$ h^{-1}). This further confirms the need for highly dispersed tungsten species in silica (Fig. 8) and a balanced ratio of Lewis and Brønsted acid sites (Fig. 9) for catalytic purposes. However, due to the increasing

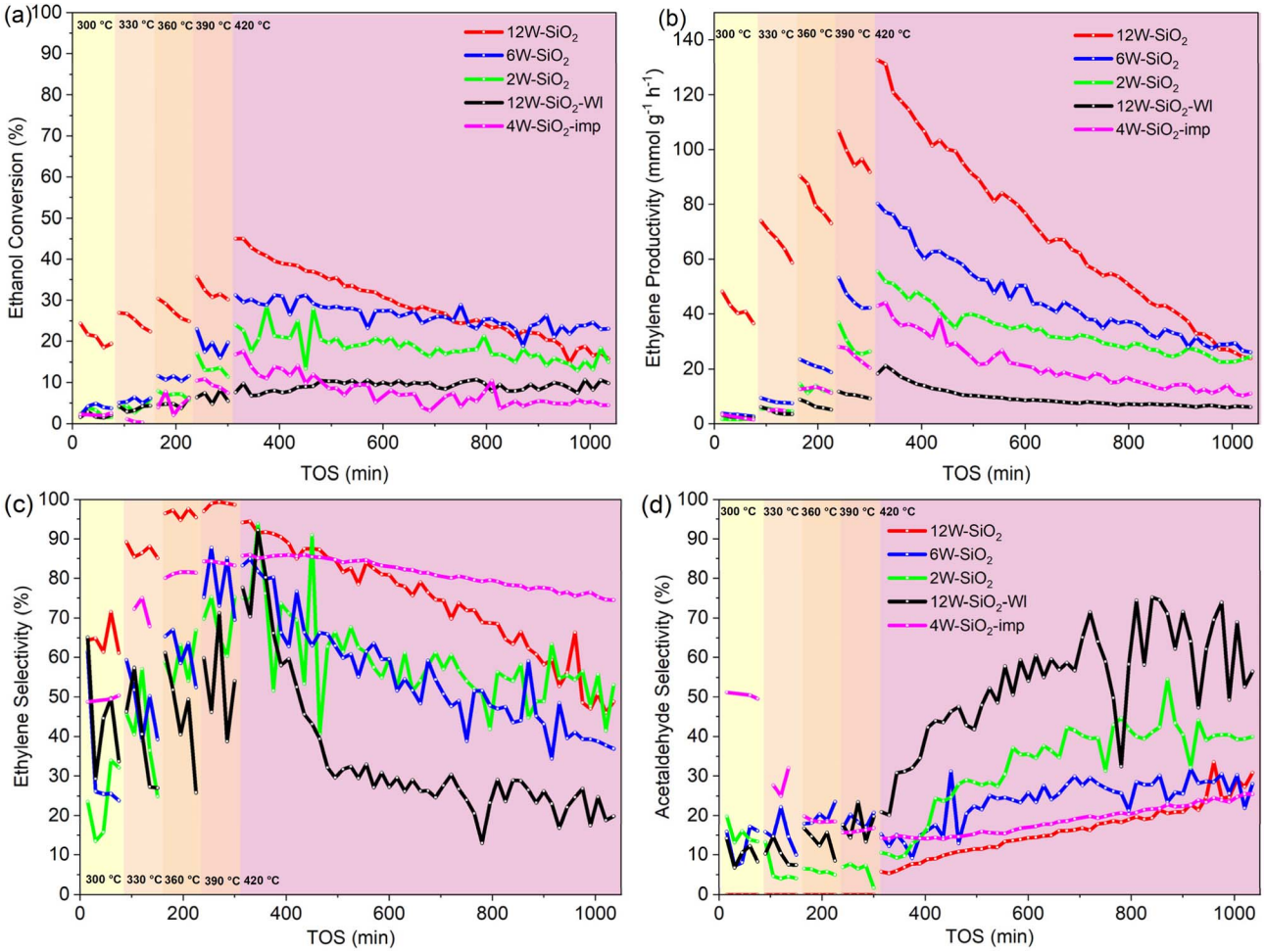

Fig. 11 Comparison of ethanol conversion (a), ethylene productivity (b), ethylene selectivity (c) and acetaldehyde selectivity (d) over W–SiO_2 microspheres with 12W–SiO_2 by wet impregnation as the reference. Catalysis was carried out at 300 to 390 °C and the stability test at 420 °C. Conditions: 50 mg of catalyst, 50 mL min^{-1} N_2, WHSV 14.19 h^{-1} of ethanol.

acetaldehyde selectivity with time-on-stream, the decrease in space-time yield is evident (Fig. 26S). The increased selectivity toward acetaldehyde for 6W–SiO_2 and, in particular, for 2W–SiO_2 can be attributed to the competitive dehydrogenation of ethanol that could be promoted by the presence of Lewis acid sites.[12,72–74]

To enhance the stability of ethanol conversion and ethylene productivity over 12W–SiO_2, inspired by Pampararo *et al.*,[75] the reaction system was co-fed with O_2 (20% of O_2 in N_2). The catalytic performance under these conditions was compared in terms of ethanol, ethylene, and acetaldehyde peak area evolution during TOS with the catalytic experiment performed in pure N_2. As illustrated in Fig. 27S, the co-feeding with O_2 led to significantly higher stability of ethanol and ethylene peak areas during TOS at 420 °C. However, as shown in Fig. 27S, a significant increase in acetaldehyde production has been observed, probably originating in the oxidative ethanol dehydrogenation pathway that has been activated in the presence of O_2.[76]

The spent catalysts were analyzed by Raman spectroscopy, XRD, SEM, XPS, and TG analysis to describe their structure and morphology after the catalytic reaction as well as their tendency to coke. The SEM image of the 12W–SiO_2 spent catalyst (Fig. 12 and 28S) shows that the microspherical morphology remained unchanged in comparison to the fresh catalyst (Fig. 4S). The Raman spectra of spent 12W–SiO_2 catalysts displayed the D and G bands characteristic of coke (Fig. 12). The Raman spectra of the spent 6W–SiO_2 and 2W–SiO_2 catalysts were affected by high fluorescence; however, weak D and G bands of carbon were observable, similar to 12W–SiO_2 (Fig. 29S). All these data suggest that coking is the primary source of deactivation in the W–SiO_2 materials presented herein, in agreement with the literature on tungsten silicate catalysts.[77]

The PXRD analysis of the spent 12W–SiO_2 catalyst revealed weak diffraction maxima corresponding to crystalline triclinic WO_3 (Fig. 29S; JCPDS card no. 01-071-0305), whereas the spent 6W–SiO_2 and 2W–SiO_2 catalysts exhibited diffraction patterns without any WO_3-related signals. The presence of WO_3 in the spent 12W–SiO_2 catalyst can be considered as an additional factor that causes deactivation of the catalyst and pronounced ethanol conversion drop. In contrast, the 6W–SiO_2 and 2W–SiO_2 catalysts without WO_3 diffractions exhibit more stable ethanol conversion.

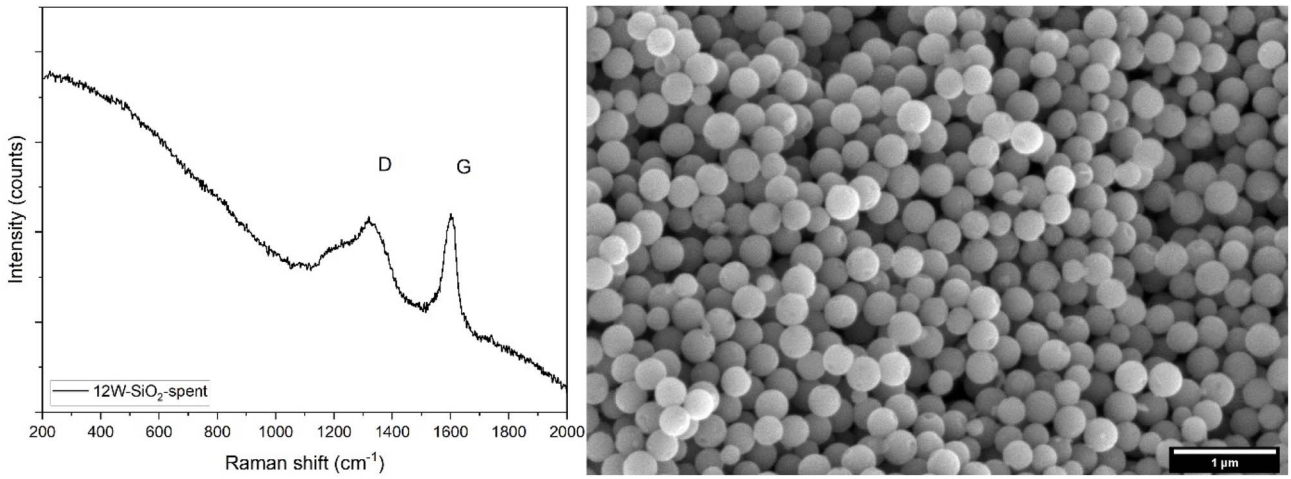

Fig. 12 Raman spectrum and SEM image of the 12W–SiO_2 spent catalyst.

The TG analysis of W–SiO_2 spent microsphere catalysts was performed to follow the decomposition of the coke generated on the catalyst surface. As illustrated in Fig. 30S the spent catalysts exhibited the maximum weight loss between 350 and 600 °C. Specifically, the mass loss for 12W–SiO_2, 6W–SiO_2, and 2W–SiO_2 spent catalyst was 12.4, 5.9, and 4.7%, respectively. According to the decomposition temperatures, the deposited carbon is mainly divided into soft coke (composed mainly of aliphatic compounds) with decomposition temperatures of 300–480 °C, and hard coke (composed mainly of aromatic compounds) with decomposition temperatures of 480–800 °C.[78] Based on this definition we can assume the presence of both soft and hard coke on the surface of spent catalysts after dehydration reactions. XPS analysis of spent catalysts (Fig. 31S–33S) shows a higher carbon content on the surface compared to the fresh catalysts (Tables 2S and 7S). The carbon content decreases with the decreasing W content. This trend corresponds to the results from TGA of spent catalysts where the highest amount of coke was observed in the case of the 12W–SiO_2 catalyst. In addition, the TGA curve of the spent 12W–SiO_2–WI catalyst (Fig. 34S) exhibited a mass loss of 6.58% showing that, even despite its low catalytic activity, coking occurred as well.

Furthermore, catalyst deactivation can be correlated with coke formation on the surface of the spent catalysts (Fig. 30S) as well as with the Brønsted acid site content in the fresh catalysts (Fig. 13).[60] It is well known that Brønsted acid sites are highly active in ethanol dehydration,[26–28,59,60] and they are largely responsible for the high initial ethanol conversion observed for the 12W–SiO_2 sample, for which the L_{py}/B_{py} ratio is 0.95 (Table 2). As the tungsten loading decreases, the relative concentration of Lewis acid sites with respect to Brønsted sites increases, leading to improved stability of ethanol conversion and lower coking.

Interestingly, the W 4f XPS spectra of spent catalysts (Fig. 33S) show a higher contribution of lower oxidation states (W^{5+})[11] than in the case of fresh catalysts (Fig. 6). Moreover, the increase in W^{5+} states (lower W^{6+}/W^{5+} ratio) is more prominent in the case of 6W–SiO_2 and 2W–SiO_2 spent catalysts (Fig. 33S and Table 8S). This behavior may be explained as a consequence of exposure of W–SiO_2 catalysts to a reductive environment (ethanol in nitrogen). Notably, samples with a lower W^{6+}/W^{5+} ratio (Table 8S) exhibited a higher selectivity to acetaldehyde at the end of catalytic tests, *i.e.*, were more active in ethanol dehydrogenation to acetaldehyde (Fig. 11d).

An additional parameter of critical relevance is the hydrophilicity of the fresh catalysts.[35,79] Because ethanol dehydration inherently generates water as a co-product, the presence of water may adversely affect catalytic activity through competitive adsorption at active sites. As shown in Fig. 10, the water adsorption isotherms confirm the intrinsically hydrophilic nature of the W–SiO_2 microspheres. Notably, water sorption measurements reveal a systematic decrease in hydrophilicity with decreasing tungsten loading (Fig. 10), which is further supported by water contact angle measurements (Fig. 21S). This behavior follows the observed catalytic performance and deactivation trends. However, it has to be considered that the hydrophilicity of

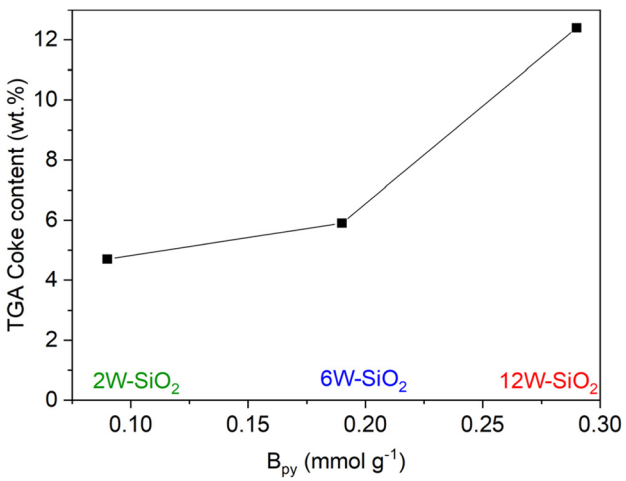

Fig. 13 Correlation between the number of Brønsted acid sites (B_{py}) and coke content in the spent catalysts.

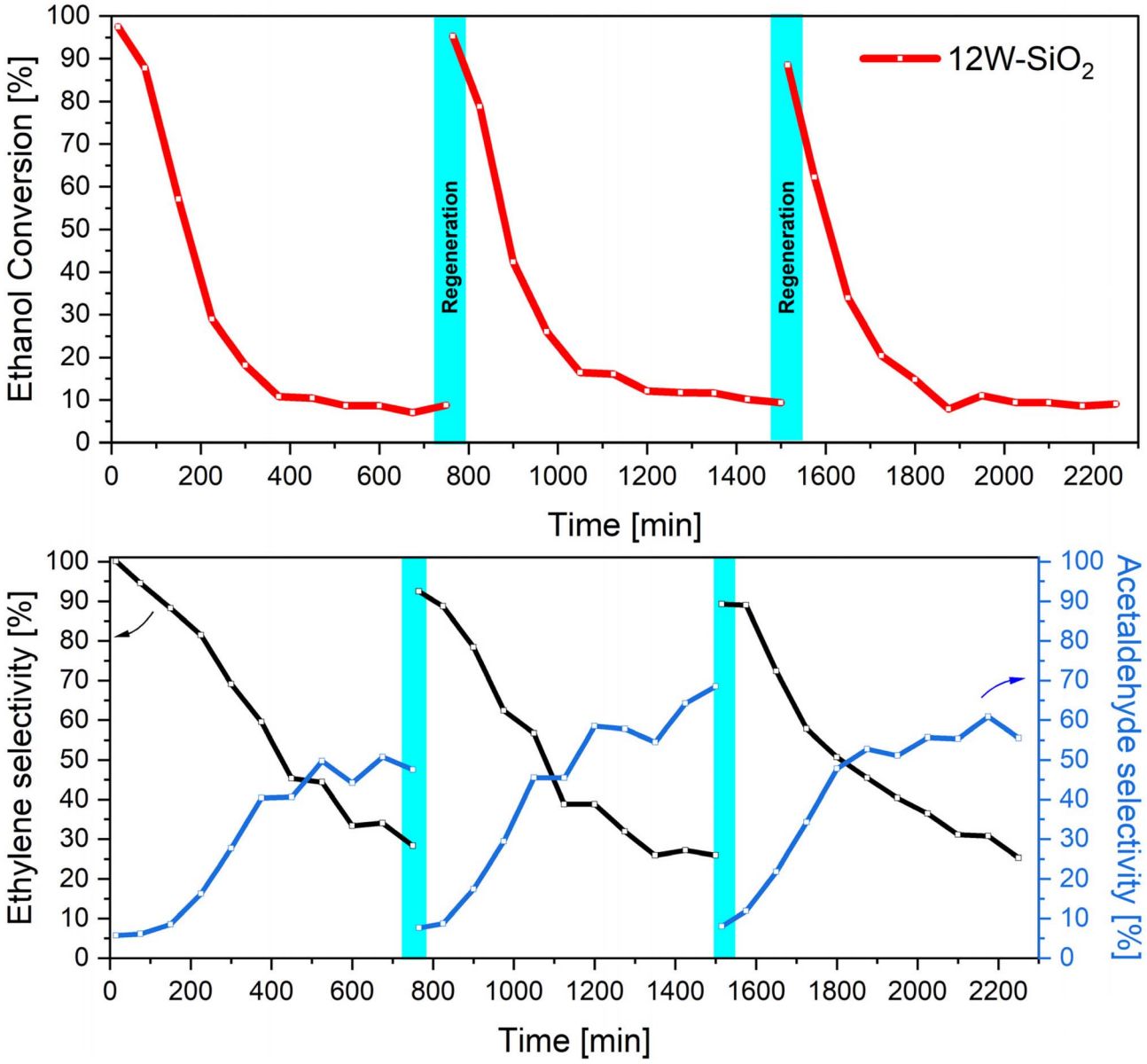

Fig. 14 Regeneration of the 12W–SiO_2 catalyst and ethanol conversions and product selectivity at 420 °C with a WHSV of 7.09 h^{-1}.

the catalysts increases with the tungsten loading and with the number of acid sites. Thus, the effect of hydrophilicity cannot be unambiguously confirmed. Based on the obtained results it can be argued that catalysts with a higher ratio of Lewis to Brønsted acid sites, combined with lower hydrophilicity, exhibit enhanced catalytic stability and reduced susceptibility to deactivation under specific reaction conditions.

To investigate the possible regeneration of the 12W–SiO_2 catalyst, three cycles of ethanol dehydration reactions at 420 °C with a WHSV of 7.09 h^{-1} were conducted in pure N_2, each of them lasting for 12 h. After the first and second runs, the catalyst was heated in a reactor bed at 500 °C in the presence of oxygen (20%) for 2 hours to remove carbon residues and re-activate the catalyst. As illustrated in Fig. 14, the catalytic activity was almost fully recovered after each regeneration step. This supports the assumption that the deactivation is caused mainly by coking. In addition, the formation of crystalline WO_3 species in 12W–SiO_2 (Fig. 29S) during the catalytic reaction must also be considered as a reason for the slightly decreasing initial ethanol conversion within each regeneration step. As frequently suggested in the literature,[35,60,79,80] the total amount of surface acid sites as well as the ratio between Lewis and Brønsted acid sites can significantly affect the catalyst's activity, selectivity, stability, and susceptibility to coking. Notably, Müller *et al.* demonstrated that a higher Lewis-to-Brønsted acid site ratio in zeolites enhanced catalytic performance in alcohol dehydration.[60] Herein, based on the presented results, it can be inferred that the Brønsted/Lewis vibrational band ratio shown in Fig. 9 and Table 2 is the highest for the 12W–SiO_2 microspheres as well as the content of Brønsted acid sites (Fig. 13),

Table 3 Catalytic performance comparison of W–SiO_2 microspheres with other relevant tungsten silicate catalysts for ethanol dehydration from the literature

Catalyst	W content [wt%]	Catalyst amount [g]	Reaction temperature [°C]	WHSV [h^{-1}]	Initial EtOH conversion [%]	Initial ethylene selectivity [%]	Ethylene productivity [mmol g^{-1} h^{-1}]	Ethylene productivity [mmol $mmol_W^{-1}$ h^{-1}]	Ref.
12W–SiO_2	11.83	0.05	420	14.19	43	100	132.62	206	This work
6W–SiO_2	6.46	0.05	420	14.19	31	83	80.21	226	This work
2W–SiO_2	1.96	0.05	420	14.19	24	75	55.61	520	This work
2W–SiO_2[a]	1.96	0.05	420	14.19	15	53	24.60	230	This work
W10KIT-6[b]	23.7	1.5	360	9.47	55.3	80.3	43.14	34	83
36-STA/SiO_2[c]	27.6	n.a.	240	9.6	86.9	60	108.73	72	1
WO_3/MCF-Si	13.5	0.1	400	3.1	99.7	95	63.81	87	13
WO_3/SBA-15	13.5	0.1	400	3.1	99	94	62.75	85	6
SiAl(HIPE)	—	—	400	11.8	99	94	327.99	—	84

[a] After 1000 min at TOS. [b] Tungsten content calculated from the $10WO_3$·$90SiO_2$ formula. [c] Reaction performed at 1 MPa.

which may be connected with a greater tendency toward coking[27,28,81] in this sample (Fig. 30S and Table 7S).

Table 3 summarizes the performance of W–SiO_2 microspheres in ethanol dehydration (Fig. 11), compared with other relevant catalysts. As illustrated, the reactions were conducted under varying conditions, which must be taken into account when evaluating the performance of different catalysts. A detailed evaluation of the data reveals that W–SiO_2 microspheres exhibit high catalytic performance in comparison to other tungsten-based catalysts. This is particularly evident when ethylene productivity is normalized either per gram of catalyst or per millimole of tungsten content. Specifically, the 2W–SiO_2 sample demonstrates the highest initial ethylene productivity based on tungsten molar content, reaching 520 mmol $mmol_W^{-1}$ h^{-1}. Notably, it maintains a high productivity of 230 mmol $mmol_W^{-1}$ h^{-1} even after 1000 minutes on stream (TOS). In terms of productivity per gram of catalyst, the 12W–SiO_2 sample achieves the highest initial value of 133 mmol g^{-1} h^{-1}, outperforming all other W-based catalysts evaluated. Overall, all W–SiO_2 microspheres show high ethylene productivity when normalized to tungsten molar content.

The comparison with other common catalysts is not straightforward. Zeolites, alumina, and amorphous aluminosilicates have mostly been tested at lower temperatures and WHSV,[27,79,80,82] hampering direct quantitative comparison. Here, hierarchically porous aluminosilicate monoliths (SiAl-(HIPE)) were tested in ethanol dehydration under reaction conditions that most closely matched those applied to the W–SiO_2 (Table 3) and exhibited a better ethylene productivity than W–SiO_2 catalysts presented herein. In addition, commercial γ-Al_2O_3 was used for comparison of catalytic activity under the same conditions as those applied to W–SiO_2 at temperatures of 300–390 °C (Fig. 23S). As expected, γ-Al_2O_3 exhibited a higher catalytic activity in terms of ethanol conversion, reaching 92% at 390 °C. Interestingly, however, the 12W–SiO_2 catalyst showed a higher selectivity toward ethylene under these conditions (98 *vs.* 94% for alumina and 12W–SiO_2 at 390 °C, respectively).

In summary, although ethanol dehydration is most commonly promoted by aluminosilicate- or alumina-based catalysts,[85] the W–SiO_2 microspheres presented here demonstrate stimulating catalytic behavior in this reaction. As demonstrated in this work, the highly homogeneous dispersion of WO_x species together with the well-defined surface acidity play a crucial role in achieving high catalytic activity compared with tungsten-based catalysts prepared *via* conventional impregnation methods (Table 3). Arguably, given that tungsten-containing catalysts are widely applied in a broad range of reactions,[8–12,46,86] the properties of the W–SiO_2 microspheres reported here may also stimulate interest in their potential use in other catalytic processes, such as olefin metathesis, olefin epoxidation, and in the upgrading of glucose or glycerol.

4 Conclusions

In this study, we report the successful one-pot sol–gel synthesis of tungsten silicate microspheres. The synthesis approach involves microwave-assisted preparation of a tungsten 2,6-

naphthalene dicarboxylate precursor solution derived from tungsten hexacarbonyl, followed by room-temperature condensation with (3-aminopropyltriethoxy)silane. This process yields hybrid tungsten silicate microspheres, which, upon calcination, form inorganic, microporous silica-based structures containing homogeneously distributed amorphous tungstate species possessing Lewis and Brønsted acidity. The uniform dispersion of tungstate is attributed to the optimized reaction conditions and sol–gel condensation, offering significant advantages over conventional impregnation methods.

Catalysts with tungsten loadings ranging from 2 to 12 wt% were evaluated for ethanol dehydration to ethylene. All samples exhibited notable activity and high selectivity, with initial ethanol conversion rates of 43%, 31%, and 24% for 12W–SiO_2, 6W–SiO_2, and 2W–SiO_2, respectively. Ethylene selectivity initially reached 100%, gradually decreasing to 65% over time on stream (TOS). Based on tungsten molar content, the 2W–SiO_2 sample showed the highest initial ethylene productivity of 520 mmol $mmol_W^{-1}$ h^{-1} (14.6 g $mmol_W^{-1}$ h^{-1}) and maintained a high value of 230 mmol $mmol_W^{-1}$ h^{-1} (6.44 g $mmol_W^{-1}$ h^{-1}) after 1000 minutes TOS, indicating good long-term catalytic stability. The 12W–SiO_2 sample achieved the highest initial ethylene productivity per gram of catalyst (133 mmol g^{-1} h^{-1}), below that of conventional (silica-)alumina-based dehydration catalysts, but clearly outperforming other tungsten–silica-based catalysts reported in the literature.

The most significant deactivation was observed for 12W–SiO_2, primarily due to coking, caused by the high amount of Brønsted acid sites. Catalysts with a lower tungsten content exhibited a lower hydrophilicity, higher L_{py}/B_{py} ratio and more stable catalytic performance. Importantly, the homogeneous dispersion of active sites was found to be a key factor in catalytic efficiency providing significantly higher activity of W–SiO_2 microspherical catalysts obtained from one-step MW-assisted sol–gel condensation compared to the 12W–SiO_2–WI and 4W–SiO_2-imp samples prepared *via* impregnation. These findings underscore the promising performance of W–SiO_2 microspheres and their potential as efficient catalysts for ethanol dehydration. Furthermore, the presence of highly dispersed tungstate active sites in these materials suggests promising applicability in heterogeneous catalysis, for example in olefin metathesis, expanding their utility beyond ethanol conversion.

Author contributions

David Skoda: conceptualization, methodology, formal analysis, investigation, validation, visualization, writing – original draft, funding acquisition, resources, project administration. Tomas Pokorny: conceptualization, methodology, investigation, formal analysis, visualization, validation, writing – review & editing. Barbora Hanulikova: investigation, formal analysis, writing – review & editing. Ales Styskalik: methodology, investigation, formal analysis, validation, writing – review & editing, resources. Zuzana Hlavenkova: investigation, visualization. Lucie Simonikova: investigation. Jan Varada: investigation. Lucie Leonova: investigation, formal analysis, visualization. Ivo Kuritka: writing – review & editing, funding acquisition, resources. Claude Poleunis: investigation, formal analysis. Damien P. Debecker: formal analysis, conceptualization, methodology, writing – review & editing, resources.

Conflicts of interest

The authors declare that they have no conflict of interest.

Data availability

The data supporting this article have been included as part of the supplementary information (SI). Supplementary information is available. See DOI: https://doi.org/10.1039/d5ta08046k.

Acknowledgements

This work was supported by project LUAUS23085, funded by the Ministry of Education, Youth and Sports of the Czech Republic (MEYS CR) within the INTER-EXCELLENCE II program. The support by the MEYS CR within the DKRVO (RP/CPS/2024-28/007) project is gratefully acknowledged. The authors acknowledge the project Quantum Materials for Applications in Sustainable Technologies (QM4ST), CZ.02.01.01/00/22_008/0004572 by Program Johannes Amos Comenius, Excellent Research call. We also acknowledge CF CryoEM and CF NMR of CIISB, Instruct-CZ Centre, supported by MEYS CR (LM2023042) and European Regional Development Fund-Project "UP CIISB" (No. CZ.02.01.01/00/23_015/0008175). CzechNanoLab project LM2023051, funded by MEYS CR, is gratefully acknowledged for the financial support of the XPS measurements at CEITEC Nano Research Infrastructure. This work was financially supported by the Grant Agency of Masaryk University (GAMU) under the grant number MUNI/A/1298/2022.

References

1 H. Li, Z. Yu, Z. Zhang, S. Li, Z. Shi, C. Ni, L. Cao, H. Du, Q.-X. Luo and F. Wang, *Ind. Eng. Chem. Res.*, 2024, **63**, 7624–7635.
2 G. Pampararo and D. P. Debecker, in *Encyclopedia of Green Chemistry*, Elsevier, 2025, pp. 304–323.
3 P. T. Benavides, U. R. Gracida-Alvarez, K. Richa, J. Port and T. R. Hawkins, *Bioresour. Technol.*, 2025, **430**, 132565.
4 C. D'Alessandro and H. Besada, in *The Palgrave Handbook of Contemporary International Political Economy*, Palgrave Macmillan UK, London, 2019, vol. 16301, pp. 377–389.
5 M. Duan, C. Hu, H. Li, Y. Chen, R. Chen, W. Gong, Z. Lu, N. Zhang, R. Long, L. Song and Y. Xiong, *JACS Au*, 2022, **2**, 1160–1168.
6 P. Trongjitraksa, Y. Klinthongchai, P. Praserthdam and B. Jongsomjit, *J. Taiwan Inst. Chem. Eng.*, 2023, **152**, 105168.
7 R. Al-Faze, A. Finch, E. F. Kozhevnikova and I. V. Kozhevnikov, *Appl. Catal., A*, 2020, **597**, 117549.
8 P. Sudarsanam, N. K. Gupta, B. Mallesham, N. Singh, P. N. Kalbande, B. M. Reddy and B. F. Sels, *ACS Catal.*, 2021, **11**, 13603–13648.

9 T. Z. H. Gani, Z. J. Berkson, R. Zhu, J. H. Kang, J. R. Di Iorio, K. W. Chan, D. F. Consoli, S. K. Shaikh, C. Copéret and Y. Román-Leshkov, *Nature*, 2023, **617**, 524–528.
10 S. Lwin and I. E. Wachs, *ACS Catal.*, 2014, **4**, 2505–2520.
11 J. J. Wiesfeld, R. Gaquere and E. J. M. Hensen, *ACS Sustain. Chem. Eng.*, 2019, **7**, 7552–7562.
12 N. V. Vlasenko, G. R. Kosmambetova, E. V. Senchylo, P. Kúš, K. Veltruská and P. E. Strizhak, *ChemSusChem*, 2025, **18**(5), e202401800.
13 P. Trongjitraksa, M. Yazdanpanah, M. Fereidooni, P. Praserthdam and B. Jongsomjit, *S. Afr. J. Chem. Eng.*, 2025, **51**, 180–187.
14 C. v. Schalkwyk, A. Spamer, D. J. Moodley, T. Dube, J. Reynhardt and J. M. Botha, *Appl. Catal., A*, 2003, **255**, 121–131.
15 P. Promchana, K. Choojun, W. Limphirat, Y. Poo-arporn and T. Sooknoi, *Appl. Catal., A*, 2023, **650**, 118972.
16 S.-H. Chai, B. Yan, L.-Z. Tao, Y. Liang and B.-Q. Xu, *Catal. Today*, 2014, **234**, 215–222.
17 M. P. Conley, V. Mougel, D. V. Peryshkov, W. P. Forrest, D. Gajan, A. Lesage, L. Emsley, C. Copéret and R. R. Schrock, *J. Am. Chem. Soc.*, 2013, **135**, 19068–19070.
18 Y. Zengin, B. Kaya, M. Safak Boroglu and I. Boz, *Ind. Eng. Chem. Res.*, 2023, **62**, 1852–1864.
19 S. Maksasithorn, P. Praserthdam, K. Suriye and D. P. Debecker, *Microporous Mesoporous Mater.*, 2015, **213**, 125–133.
20 S. Maksasithorn, P. Praserthdam, K. Suriye, M. Devillers and D. P. Debecker, *Appl. Catal., A*, 2014, **488**, 200–207.
21 D. P. Debecker, M. Stoyanova, U. Rodemerck, F. Colbeau-Justin, C. Boissère, A. Chaumonnot, A. Bonduelle and C. Sanchez, *Appl. Catal., A*, 2014, **470**, 458–466.
22 Y. Tao, O. De Luca, B. Singh, A. J. Kamphuis, J. Chen, P. Rudolf and P. P. Pescarmona, *Mater. Today Chem.*, 2020, **18**, 100373.
23 A. Guntida, K. Suriye, J. Panpranot and P. Praserthdam, *Catal. Today*, 2020, **358**, 354–369.
24 S. Boonpai, S. Wannakao, J. Panpranot, B. Jongsomjit and P. Praserthdam, *J. Phys. Chem. C*, 2020, **124**, 15935–15943.
25 J. González, J. A. Wang, L. F. Chen, M. E. Manríquez and J. M. Dominguez, *J. Phys. Chem. C*, 2017, **121**, 23988–23999.
26 P. Kerdnoi, C. Autthanit, N. Chitpong and B. Jongsomjit, *Bull. Chem. React. Eng. Catal.*, 2020, **15**, 96–103.
27 A. Styskalik, V. Vykoukal, L. Fusaro, C. Aprile and D. P. Debecker, *Appl. Catal. B Environ.*, 2020, **271**, 118926.
28 C. P. Nash, A. Ramanathan, D. A. Ruddy, M. Behl, E. Gjersing, M. Griffin, H. Zhu, B. Subramaniam, J. A. Schaidle and J. E. Hensley, *Appl. Catal., A*, 2016, **510**, 110–124.
29 V. Zacharopoulou and A. Lemonidou, *Catalysts*, 2017, **8**, 2.
30 P. González-Navarrete, M. Schlangen, X. Wu and H. Schwarz, *Chem.–Eur. J.*, 2016, **22**, 3077–3083.
31 M. Duan, C. Hu, H. Li, Y. Chen, R. Chen, W. Gong, Z. Lu, N. Zhang, R. Long, L. Song and Y. Xiong, *JACS Au*, 2022, **2**, 1160–1168.
32 S. Lwin, Y. Li, A. I. Frenkel and I. E. Wachs, *ACS Catal.*, 2016, **6**, 3061–3071.
33 R. B. Demuner, J. G. Soares Santos Maia, A. R. Secchi, P. A. Melo, R. W. do Carmo and G. S. Gusmão, *Ind. Eng. Chem. Res.*, 2019, **58**, 2717–2726.
34 A. I. Osman, J. K. Abu-Dahrieh, A. Abdelkader, N. M. Hassan, F. Laffir, M. McLaren and D. Rooney, *J. Phys. Chem. C*, 2017, **121**, 25018–25032.
35 A. Styskalik, I. Kordoghli, C. Poleunis, A. Delcorte, Z. Moravec, L. Simonikova, V. Kanicky, C. Aprile, L. Fusaro and D. P. Debecker, *J. Mater. Chem. A*, 2020, **8**, 23526–23542.
36 B. T. Loc, L. N. Q. Tu and N. Q. Long, *Vietnam J. Catal. Adsorpt.*, 2021, **10**, 79–83.
37 D. Skoda, B. Hanulikova, A. Styskalik, V. Vykoukal, P. Machac, P. Urbanek, E. Domincova Bergerova, L. Simonikova and I. Kuritka, *J. Ind. Eng. Chem.*, 2022, **107**, 320–332.
38 D. Skoda, R. Zhu, B. Hanulikova, A. Styskalik, V. Vykoukal, P. Machac, L. Simonikova, I. Kuritka, C. Poleunis, D. P. Debecker and Y. Román-Leshkov, *ACS Catal.*, 2023, **13**, 12970–12982.
39 D. Skoda, K. Kuzelova, R. B. Pricilla, B. Hanulikova, M. Urbanek, A. Styskalik, T. Pokorny, I. Doroshenko, L. Simonikova and I. Kuritka, *J. Ind. Eng. Chem.*, 2025, **148**, 502–513.
40 R. López and R. Gómez, *J. Sol-Gel Sci. Technol.*, 2012, **61**, 1–7.
41 M. Jacquemin, M. J. Genet, E. M. Gaigneaux and D. P. Debecker, *ChemPhysChem*, 2013, **14**, 3618–3626.
42 N. Fairley, V. Fernandez, M. Richard-Plouet, C. Guillot-Deudon, J. Walton, E. Smith, D. Flahaut, M. Greiner, M. Biesinger, S. Tougaard, D. Morgan and J. Baltrusaitis, *Appl. Surf. Sci. Adv.*, 2021, **5**, 100112.
43 S. Lowell, J. E. Shields, M. A. Thomas and M. Thommes, in *Characterization of Porous Solids and Powders: Surface Area, Pore Size and Density*, Springer Netherlands, 2004, pp. 58–81.
44 M. Luisa Ojeda, J. Marcos Esparza, A. Campero, S. Cordero, I. Kornhauser and F. Rojas, *Phys. Chem. Chem. Phys.*, 2003, **5**, 1859.
45 E. I. Ross-Medgaarden and I. E. Wachs, *J. Phys. Chem. C*, 2007, **111**, 15089–15099.
46 E. Mazoyer, N. Merle, A. De Mallmann, J.-M. Basset, E. Berrier, L. Delevoye, J.-F. Paul, C. P. Nicholas, R. M. Gauvin and M. Taoufik, *Chem. Commun.*, 2010, **46**, 8944.
47 T. Takkawatakarn, K. Suriye, B. Jongsomjit, J. Panpranot and P. Praserthdam, *Catal. Today*, 2020, **358**, 345–353.
48 A. V. Colusso, A. McDonagh and M. B. Cortie, *Surf. Interface Anal.*, 2018, **50**, 1384–1388.
49 Y. Liu, S. Shrestha and W. E. Mustain, *ACS Catal.*, 2012, **2**, 456–463.
50 K. M. McCreary, A. T. Hanbicki, G. G. Jernigan, J. C. Culbertson and B. T. Jonker, *Sci. Rep.*, 2016, **6**, 19159.
51 N. Minh Vuong, D. Kim and H. Kim, *Sci. Rep.*, 2015, **5**, 11040.
52 Q. Xin, L. Jiang, S. Yu, S. Liu, D. Yin, L. Li, C. Xie, Q. Wu, H. Yu, Y. Liu and Y. Liu, *J. Phys. Chem. C*, 2021, **125**, 18170–18179.
53 J. G. Howell, Y.-P. Li and A. T. Bell, *ACS Catal.*, 2016, **6**, 7728–7738.

54 D. P. Debecker, B. Schimmoeller, M. Stoyanova, C. Poleunis, P. Bertrand, U. Rodemerck and E. M. Gaigneaux, *J. Catal.*, 2011, **277**, 154–163.
55 R. De Clercq, M. Dusselier, C. Poleunis, D. P. Debecker, L. Giebeler, S. Oswald, E. Makshina and B. F. Sels, *ACS Catal.*, 2018, **8**, 8130–8139.
56 L.-T. Weng, *Appl. Catal., A*, 2014, **474**, 203–210.
57 E. L. Lee and I. E. Wachs, *J. Phys. Chem. C*, 2007, **111**, 14410–14425.
58 C. Martín, P. Malet, G. Solana and V. Rives, *J. Phys. Chem. B*, 1998, **102**, 2759–2768.
59 B. Li, K. Leng, Y. Zhang, J. J. Dynes, J. Wang, Y. Hu, D. Ma, Z. Shi, L. Zhu, D. Zhang, Y. Sun, M. Chrzanowski and S. Ma, *J. Am. Chem. Soc.*, 2015, **137**, 4243–4248.
60 J. M. Müller, G. C. Mesquita, S. M. Franco, L. D. Borges, J. L. de Macedo, J. A. Dias and S. C. L. Dias, *Microporous Mesoporous Mater.*, 2015, **204**, 50–57.
61 C. A. Emeis, *J. Catal.*, 1993, **141**, 347–354.
62 V. Zholobenko, C. Freitas, M. Jendrlin, P. Bazin, A. Travert and F. Thibault-Starzyk, *J. Catal.*, 2020, **385**, 52–60.
63 J. M. R. Gallo, C. Bisio, G. Gatti, L. Marchese and H. O. Pastore, *Langmuir*, 2010, **26**, 5791–5800.
64 G. Rother, A. G. Stack, S. Gautam, T. Liu, D. R. Cole and A. Busch, *J. Phys. Chem. C*, 2020, **124**, 15188–15194.
65 S. W. Rutherford, *Langmuir*, 2025, **41**, 25086–25099.
66 S. W. Rutherford, *Langmuir*, 2025, **41**, 20502–20515.
67 K. Zhang, R. P. Lively, J. D. Noel, M. E. Dose, B. A. McCool, R. R. Chance and W. J. Koros, *Langmuir*, 2012, **28**, 8664–8673.
68 M. Thommes, S. Mitchell and J. Pérez-Ramírez, *J. Phys. Chem. C*, 2012, **116**, 18816–18823.
69 P. B. Weisz and C. D. Prater, Interpretation of Measurements in Experimental Catalysis, in *Advances in Catalysis*, 1954, pp. 143–196.
70 F. Schüth, M. D. Ward and J. M. Buriak, *Chem. Mater.*, 2018, **30**, 3599–3600.
71 C. Perego, *Catal. Today*, 1999, **52**, 133–145.
72 J. F. DeWilde, C. J. Czopinski and A. Bhan, *ACS Catal.*, 2014, **4**, 4425–4433.
73 Y. Zhang, L. Qi, Y. Li, T. Yang, D. M. Meira, C. Dun, H. Hu, H. Chen, S. Xu, J. J. Urban, A. D. Sadow, T. Kobayashi, L. Qi, P. Tian and A. T. Bell, *ACS Catal.*, 2024, **14**, 15204–15220.
74 Q. Meng, F. Chen, X. Li, C. Qiu, Q. Yuan and T. Wang, *J. Catal.*, 2026, **453**, 116571.
75 G. Pampararo, Z. Hlavenková, A. Styskalik and D. P. Debecker, *Catal. Sci. Technol.*, 2024, **14**, 4912–4926.
76 J. Pang, M. Yin, P. Wu, X. Li, H. Li, M. Zheng and T. Zhang, *Green Chem.*, 2021, **23**, 7902–7916.
77 O. Verdes, V. Sasca, A. Popa, M. Suba and S. Borcanescu, *Catal. Today*, 2021, **366**, 123–132.
78 Y. Sun, L. Wei, Z. Zhang, H. Zhang and Y. Li, *Energy Fuels*, 2023, **37**, 1657–1677.
79 L. Leonova, Z. Moravec, P. Sazama, J. Pastvova, L. Kobera, J. Brus and A. Styskalik, *ChemCatChem*, 2023, **15**(13), e202300449.
80 T. K. Phung and G. Busca, *Catal. Commun.*, 2015, **68**, 110–115.
81 J. Bi, X. Guo, M. Liu and X. Wang, *Catal. Today*, 2010, **149**, 143–147.
82 A. Styskalik, I. Kordoghli, C. Poleunis, A. Delcorte, C. Aprile, L. Fusaro and D. P. Debecker, *Microporous Mesoporous Mater.*, 2020, **297**, 110028.
83 H. Zhu, A. Ramanathan, J.-F. Wu and B. Subramaniam, *ACS Catal.*, 2018, **8**, 4848–4859.
84 D. P. Debecker, C. Boissière, G. Laurent, S. Huet, P. Eliaers, C. Sanchez and R. Backov, *Chem. Commun.*, 2015, **51**, 14018–14021.
85 T. K. Phung, L. Proietti Hernández, A. Lagazzo and G. Busca, *Appl. Catal., A*, 2015, **493**, 77–89.
86 D. Hoegaerts, B. F. Sels, D. E. De Vos, F. Verpoort and P. A. Jacobs, *Catal. Today*, 2000, **60**, 209–218.